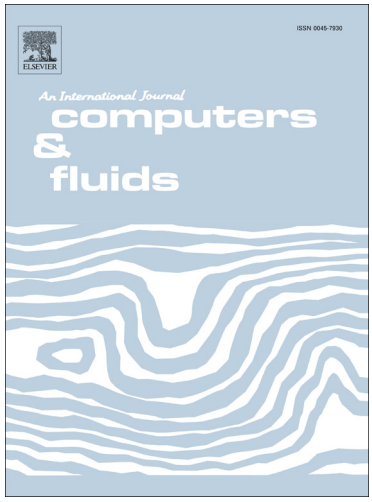

A simple HLLC-type Riemann solver for compressible non-equilibrium two-phase flows

Damien Furfaro, Richard Saurel

PII: S0045-7930(15)00025-0
DOI: http://dx.doi.org/10.1016/j.compfluid.2015.01.016
Reference: CAF 2795

To appear in: *Computers & Fluids*

Received Date: 3 December 2014
Revised Date: 16 January 2015
Accepted Date: 30 January 2015

Please cite this article as: Furfaro, D., Saurel, R., A simple HLLC-type Riemann solver for compressible non-equilibrium two-phase flows, *Computers & Fluids* (2015), doi: http://dx.doi.org/10.1016/j.compfluid.2015.01.016

A simple HLLC-type Riemann solver for compressible non-equilibrium two-phase flows

Damien Furfaro [(1)] **and Richard Saurel** [(1,2)]

[(1)]Aix-Marseille University, IUSTI UMR CNRS 7343, 5 rue E. Fermi, 13453 Marseille Cedex 13, France

[(2)] RS2N SAS, 371 chemin de Gaumin, 83640 Saint-Zacharie, France

Abstract

A simple, robust and accurate HLLC-type Riemann solver for two-phase 7-equation type models is built. It involves 4 waves per phase, i.e. the three conventional right- and left-facing and contact waves, augmented by an extra "interfacial" wave. Inspired by the Discrete Equations Method (Abgrall and Saurel, 2003), this wave speed (u_I) is assumed function only of the piecewise constant initial data. Therefore it is computed easily from these initial states. The same is done for the interfacial pressure P_I. Interfacial variables u_I and P_I are thus local constants in the Riemann problem. Thanks to this property there is no difficulty to express the non-conservative system of partial differential equations in local conservative form. With the conventional HLLC wave speed estimates and the extra interfacial speed u_I, the four-waves Riemann problem for each phase is solved following the same strategy as in Toro et al. (1994) for the Euler equations. As u_I and P_I are functions only of the Riemann problem initial data, the two-phase Riemann problem consists in two independent Riemann problems with 4 waves only. Moreover, it is shown that these solvers are entropy producing. The method is easy to code and very robust. Its accuracy is validated against exact solutions as well as experimental data.

Corresponding author: Richard Saurel
phone number: 09 72 45 86 94
email: Richard.Saurel@univ-amu.fr

1. Introduction

This paper deals with the building of an approximate HLLC-type Riemann solver for hyperbolic two-phase non-equilibrium flows. It exists a wide range of physical and industrial applications where phase compressibility is mandatory (detonations, phase change, explosions ..) in conjunction with velocity disequilibrium. In this frame Baer and Nunziato (1986) type models are hyperbolic, this property being important with respect to the causality principle. To be more precise, the present work considers the Saurel et al. (2003) symmetric variant of Baer and Nunziato (BN) model. It involves 7 wave speeds instead of 6, this detail having importance as will be examined further.

BN-type models correspond to hyperbolic systems of partial differential equations (PDEs) with 7 equations, each phase having its own set of mass, momentum and energy balance equations. The seventh equation expresses the volume fraction transport, with the transport velocity u_I and involves a pressure relaxation term. Each phase evolves with its own density, velocity and pressure, in its own sub-volume.

This type of hyperbolic system involves many fundamental difficulties for the derivation of numerical methods. First, many non-linear waves are present (6 or 7) rendering complex the Riemann problem solution determination. Second, non-conservative terms are present as well as stiff relaxation terms. They both render difficult the determination of jump relations across waves.

The first Godunov type scheme developed for these equations is due to Saurel and Abgrall (1999) where the Riemann problem solution is approximated in the two-wave HLL context. Non-conservative terms are solved consistently with the fluxes approximation. This method is simple and robust, but too dissipative and unable to handle steady contact discontinuities.

The BN system Riemann problem has been studied by Andrianov and Warnecke (2004) in an 'inverse' context as the solution is anticipated and initial data rebuilt. A 3-wave HLLC-type solver was proposed by Li et al. (2004), restricted however to flows in mechanical equilibrium, i.e. in the limit of stiff pressure and velocity relaxation (Lallemand and Saurel, 2000), resulting in the single velocity flow model of Kapila et al. (2001).

Schwendeman et al. (2006) have built a 6-wave exact-type Riemann solver for the BN model with the help of a regularization method for the interfacial wave. Indeed, in the BN model, a regularization is needed as the interfacial wave is degenerate. Deledicque and Papalexandris (2007) developed another exact-type Riemann solver without regularization and gave existence conditions for the solution. Dumbser et al. (2010) considered

the central scheme (FORCE solver) of Toro and Billet (2000) with the regularisation method of Parés (2006) for non-conservative terms. The method was developed in the frame of very high order schemes in conjunction with 3D unstructured meshes, producing impressive results (Dumbser et al., 2010). The method was improved again in Dumbser and Toro (2011) with an upwind solver based on Osher and Solomon (1982) method with 5 intermediate states in the Riemann problem. The regularisation method of Parés (2006) was still used for non-conservative terms. Tokareva and Toro (2010) also developed a HLLC-type Riemann solver with 6 waves and 5 intermediate states.

Ambroso et al. (2012) considered a BN-type model with 7 waves instead of 6, resulting in an algorithm free of regularization method. Such extended BN-type model was proposed by Saurel et al. (2003) with 'interfacial' pressure and velocity estimates issued of the acoustic Riemann solver for the Euler equations. The present contribution follows the same lines regarding this specific point. Last, Liang et al. (2014) reconsidered the 3-wave HLLC solver of Li et al. (2004), still in the context of mechanical equilibrium solutions, i.e. in conjunction with stiff mechanical relaxation solvers, in the frame of GPU computing.

Generally speaking, these methods are restricted to flows in mechanical equilibrium or to flows with velocity disequilibrium but with extra restrictions. These restrictions can be for example low volume fraction jumps. In the authors knowledge, there is no evidence that these solvers are robust enough for flows in severe conditions, such as in detonations and explosions in the presence of stiff volume fraction gradients such as those appearing at material interfaces, in conjunction with both high velocity drift and high pressure gradients. To deal with both interfacial flows and multiphase non-equilibrium mixtures in a unique formulation, robust in drastic conditions Abgrall and Saurel (2003) developed another approach. In the aforementioned methods, the Riemann problem is considered for given systems of PDEs, as done conventionally. A non-conventional method was derived by Abgrall and Saurel (2003) following the basic ideas of the Godunov method for the Euler equations. The first version of the Godunov method considers cell averaging of Riemann problem solutions. See Toro (1997) for details and Toro (1989) for second-order extension. In Abgrall and Saurel (2003) the two-phase computational cell is divided in two sub volumes, each one corresponding to a given phase. At each phase cell boundaries the Riemann problem for the Euler equations is solved. These solutions are then averaged in each sub-volume and provide a set of discrete equations that correspond to some kind of two-phase Godunov method (Discrete Equations Method – DEM). In the continuous limit, when both space and time steps tend to

zero, a BN-type model is recovered, as shown in Saurel et al. (2003). This model variant has 7 waves, is hyperbolic, symmetric in the sense that indexes of the phase can be reversed without changing the results and is in agreement with the second law of thermodynamics.

The DEM method is also both accurate and robust. It has been successfully applied to material interfaces (Abgrall and Saurel, 2003), detonation waves in heterogeneous explosives (Chinnayya et al., 2004), cavitation around hypervelocity underwater bodies (Le Metayer et al., 2005), shocks in multiphase mixtures (Saurel et al., 2007) and two-phase nozzle flows (Berry et al., 2010). A variant of this method was derived by Chang and Liou (2007). Its ability to deal with phase transition fronts with the help of thermochemical relaxation solvers was demonstrated in Zein et al. (2010).

One of the reasons for this robustness is that non-conservative products are unambiguously solved by a physical wave diffraction problem. For instance, when a shock interacts with a volume fraction discontinuity, the product of Heaviside and Dirac functions appear. However, as soon as interaction occurs, the shock wave is diffracted in a weaker transmitted shock and reflected expansion wave (local Riemann problem of the Euler equations). As the pressure and velocity in the diffracted region are constants, the product with the Dirac function (volume fraction gradient) is unambiguous. This remark is at the core of the treatment of non-conservative terms with the DEM.

However, this method is not so easy to implement and is quite computational expensive. These two arguments are the motivation of the present work where a simplified method, easier to implement, faster and even more robust is developed.

From the DEM, we have learnt an important fact: The interfacial velocity is fairly approximated as a function only of the initial data at phase contacts separating two phases (contacts 1-2 or 2-1) as shown in Figure 1. In this figure, the interface velocity is determined as solution of the Riemann problem for the Euler equations, with initial data corresponding to two fluids separated by an interface, fluid 1 on the left and fluid 2 on the right. The same remark is valid for the interfacial pressure.

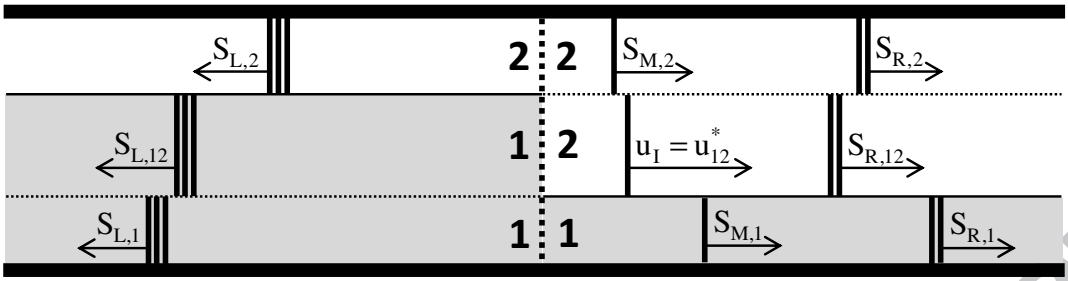

Figure 1: Stratified flow reference topology used in the DEM. Each flow channel (1-1, 1-2 and 2-2) sets in contact the phases, that involve initial discontinuities separating the left (L) and right (R) states. From these initial discontinuities, wave emerge and propagate in the various channels with their own speeds (S_L, S_R and S_M) as well as u_I, the local interfacial velocity. This cell boundary representation used in the DEM assumes 1D flow in each channel during the hyperbolic step. Multi-D effects are considered through relaxation terms.

A second major fact also appeared from the equations structure and DEM method. In this method, the channels 1-1, 1-2, 2-1 and 2-2 are considered frozen during wave propagation: Their height is constant during the hyperbolic step, meaning that corresponding volume fractions are locally frozen. In terms of continuous model, it means that relaxation effects are removed from the equations at each cell boundary, as done usually with Riemann solvers. Physically, it means that 2D effects in wave propagation and interface motion are locally omitted, as they are summarized in pressure relaxation effects.

Thanks to the two assumptions,

- local constancy of u_I and p_I,
- local freezing of volume fractions, or more precisely, volume fractions variations occurring only across u_I,

two major consequences result.

First, it is possible to express the two-phase model in local conservative form.

Second, each phase becomes decoupled from the other and has its own 4-wave Riemann solver.

These two properties render quite easy the development of HLLC-type Riemann solvers for the velocity and pressure non-equilibrium flow model. This solver is then analysed and is shown to be in agreement with the

second law of thermodynamics. Several test problems are then addressed, showing method accuracy and robustness with respect to configurations having either exact solutions or experimental reference data.

The paper is organized as follows. The model under examination, with seven equations and seven waves is presented in Section 2. The issue of interfacial variables that are considered locally constant is addressed in Section 3 together with the local conservative formulation. The two-phase Riemann solver is built in Section 4. Its agreement with the second law of thermodynamics is addressed in Section 5. A simple Godunov type scheme is built in Section 6 and validation results are shown in Section 7.

2. Two-phase flow model and properties

The starting point of the analysis is a variant of the BN model derived from the DEM. Taking the continuous limit of these discrete equations (Saurel et al., 2003) the following set of PDEs has been obtained:

Phase1

$$\frac{\partial \alpha_1}{\partial t} + u_I \frac{\partial \alpha_1}{\partial x} = \mu(P_1 - P_2)$$

$$\frac{\partial \alpha_1 \rho_1}{\partial t} + \frac{\partial \alpha_1 \rho_1 u_1}{\partial x} = 0$$

$$\frac{\partial \alpha_1 \rho_1 u_1}{\partial t} + \frac{\partial \alpha_1 \rho_1 u_1^2 + \alpha_1 P_1}{\partial x} = P_I \frac{\partial \alpha_1}{\partial x} + \lambda(u_2 - u_1) \qquad (1)$$

$$\frac{\partial \alpha_1 \rho_1 E_1}{\partial t} + \frac{\partial \alpha_1 (\rho_1 E_1 + P_1) u_1}{\partial x} = P_I u_I \frac{\partial \alpha_1}{\partial x} + \lambda \overline{u_I}(u_2 - u_1) - \mu \overline{P_I}(P_1 - P_2)$$

Phase2

$$\frac{\partial \alpha_2 \rho_2}{\partial t} + \frac{\partial \alpha_2 \rho_2 u_2}{\partial x} = 0$$

$$\frac{\partial \alpha_2 \rho_2 u_2}{\partial t} + \frac{\partial \alpha_2 \rho_2 u_2^2 + \alpha_2 P_2}{\partial x} = P_I \frac{\partial \alpha_2}{\partial x} - \lambda(u_2 - u_1)$$

$$\frac{\partial \alpha_2 \rho_2 E_2}{\partial t} + \frac{\partial \alpha_2 (\rho_2 E_2 + P_2) u_2}{\partial x} = P_I u_I \frac{\partial \alpha_2}{\partial x} - \lambda \overline{u_I}(u_2 - u_1) + \mu \overline{P_I}(P_1 - P_2)$$

This model considers each phase as compressible, evolving with its own velocity, temperature and pressure. Here, heat and mass transfers, as well as body forces have been omitted. The notations are conventional in the two-phase flow literature. The variable α_k represents the volume fraction of phase k, such that $\sum_k \alpha_k = 1$. ρ

, u , P, e and E represent respectively the density, the velocity, the pressure, the internal energy and the total energy ($E = e + \frac{1}{2}u^2$).

The interfacial variables are symmetric with respect to the phase's indexes,

$$u_I = \frac{Z_1 u_1 + Z_2 u_2}{Z_1 + Z_2} + \mathrm{sgn}\left(\frac{\partial \alpha_1}{\partial x}\right)\frac{P_2 - P_1}{Z_1 + Z_2}, \quad (2)$$

$$P_I = \frac{Z_2 P_1 + Z_1 P_2}{Z_1 + Z_2} + \mathrm{sgn}\left(\frac{\partial \alpha_1}{\partial x}\right)\frac{Z_1 Z_2}{Z_1 + Z_2}(u_2 - u_1), \quad (3)$$

where $Z_k = \rho_k c_k$ represents the acoustic impedance of phase k with c_k the associated sound speed.

These interfacial variables control the dynamics of droplet clouds, as they express velocity transport and forces acting at volume fraction gradients.

The volume average pressure and interface velocity are given by,

$$\overline{u_I} = \frac{Z_1 u_1 + Z_2 u_2}{Z_1 + Z_2}, \ \overline{P_I} = \frac{Z_2 P_1 + Z_1 P_2}{Z_1 + Z_2}.$$

These variables express the transport velocity and pressure force inside the cloud of droplets.

The mechanical equilibrium state is reached at the end of relaxation processes controlled by the following rates,

$\mu = \frac{A_I}{Z_1 + Z_2}$, the pressure relaxation rate, where A_I represents the specific interfacial area,

$\lambda = \frac{1}{2}\mu Z_1 Z_2$, the velocity relaxation rate (or 'acoustic' drag) due to pressure forces.

Viscous effects can be added to this drag coefficient.

The thermodynamic closure of System (1) is achieved by convex equations of state $e_k = e_k(P_k, \rho_k)$.

The model fulfils the second law of thermodynamics, as the entropy equations read,

$$\frac{\partial \alpha_1 \rho_1 s_1}{\partial t} + \frac{\partial \alpha_1 \rho_1 u_1 s_1}{\partial x} =$$
$$\frac{1}{T_1}\left\{ \frac{Z_1}{(Z_1+Z_2)^2}\left((P_2-P_1) + \mathrm{sgn}\left(\frac{\partial \alpha_1}{\partial x}\right) Z_2 (u_2-u_1) \right)^2 \left|\frac{\partial \alpha_1}{\partial x}\right| + \lambda \frac{Z_2}{Z_1+Z_2}(u_2-u_1)^2 + \mu \frac{Z_1}{Z_1+Z_2}(P_2-P_1)^2 \right\}$$
$$\frac{\partial \alpha_2 \rho_2 s_2}{\partial t} + \frac{\partial \alpha_2 \rho_2 u_2 s_2}{\partial x} =$$
$$\frac{1}{T_2}\left\{ \frac{Z_2}{(Z_1+Z_2)^2}\left((P_2-P_1) + \mathrm{sgn}\left(\frac{\partial \alpha_1}{\partial x}\right) Z_2 (u_2-u_1) \right)^2 \left|\frac{\partial \alpha_2}{\partial x}\right| + \lambda \frac{Z_1}{Z_1+Z_2}(u_2-u_1)^2 + \mu \frac{Z_2}{Z_1+Z_2}(P_2-P_1)^2 \right\}$$

The right hand side of these two equations being positive or null, the mixture entropy production is necessarily positive too. Moreover, the system is hyperbolic with wave speeds u_I, $u_k \pm c_k$ and u_k for $k = 1,2$.

System (1) in the absence of source terms can be cast in compact form as:

$$\frac{\partial U_k}{\partial t} + \frac{\partial F_k}{\partial x} + \alpha_k \frac{\partial H_k}{\partial x} = 0, \ \forall k \in \{1,2\} \tag{4}$$

with $U_k = \begin{pmatrix} \alpha_k \\ (\alpha\rho)_k \\ (\alpha\rho u)_k \\ (\alpha\rho E)_k \end{pmatrix}$; $F_k = \begin{pmatrix} \alpha_k u_I \\ (\alpha\rho u)_k \\ \alpha_k (\rho u^2 + P)_k - \alpha_k P_I \\ \alpha_k (\rho E + P)_k u_k - \alpha_k P_I u_I \end{pmatrix}$ and $H_k = \begin{pmatrix} -u_I \\ 0 \\ P_I \\ P_I u_I \end{pmatrix}$.

3. Local constants and local conservative formulation

It is now important to examine more closely the interfacial variables u_I and P_I that appear in the vectors F_k and H_k. To understand their meaning, the basic ideas of the DEM are re-examined.

3.1 DEM basis

This method consists in integrating Riemann problem solutions of the Euler equations on a given two-phase flow topology. The 1D Euler equations are expressed hereafter in condensed form as,

$$\frac{\partial w}{\partial t} + \frac{\partial f}{\partial x} = 0,$$

with, $w = (\rho, \quad \rho u, \quad \rho E)^T$ and $f = (\rho u, \quad \rho u^2 + P, \quad (\rho E + P)u)^T$.

The building of the discrete system with the DEM needs a two-phase topology as input, the simplest being the stratified flow one, as shown in Figure 1. Other topologies have been considered, such as annular flows in

Saurel et al. (2003) and granular flows in Chinnayya et al. (2004). The discrete system has been shown as topology independent regarding the discrete form of (4). Only relaxation terms, that are not considered here, are topology dependent.

As shown in Figure 1, at each cell boundary four types of contact are possible between fluids $l \in \{1,2\}$ at left and fluids $m \in \{1,2\}$ at right: '1-1', '2-1', '2-2' and '1-2'. Each flow channel is solved independently of the others and has height h_{lm}, constant during the hyperbolic step. It means that volume fractions are locally frozen. It also means that wave dynamics and interface motion are assumed 1D, multi-D effects being considered in relaxation effects, omitted during the Riemann problem resolution.

The DEM uses Eulerian fluxes f^{*}_{lm} and Lagrangian ones $f^{Lag,*}_{lm} = \left(f - u_l w\right)^{*}_{lm}$. For each contact 'l-m' the Riemann problem of the Euler equation is solved to compute these fluxes. For example, considering the cell boundary $i-1/2$, the Eulerian flux for the l-m contact is computed as $f^{*}_{lm} = f^{*}_{lm}\left(w^{n}_{l,i-1}, w^{n}_{m,i}\right)$, where the superscript n denotes the time step. In the same way, the Lagrangian flux is obtained as $f^{Lag*}_{lm} = f^{Lag*}_{lm}\left(w^{n}_{l,i-1}, w^{n}_{m,i}\right)$.

The DEM discrete scheme for phase k then reads,

$$\frac{\left(U_k\right)^{n+1}_{i} - \left(U_k\right)^{n}_{i}}{\Delta t} + \frac{F^{Eul,k}_{i+1/2} - F^{Eul,k}_{i-1/2}}{\Delta x} = \frac{F^{Lag,k}_{i+1/2} + F^{Lag,k}_{i-1/2}}{\Delta x},$$

where Δx represents the space step, Δt the time step and the two-phase fluxes, for phase 1 (symmetric formulas being obtained for the second phase) are given by,

$$F^{Eul,1}_{i-1/2} = h_{11} f^{*}_{11}\left(w^{n}_{1,i-1}, w^{n}_{1,i}\right) + \frac{u^{*,+}_{12}}{\left|u^{*}_{12}\right|} h_{12} f^{*}_{12}\left(w^{n}_{1,i-1}, w^{n}_{2,i}\right) - \frac{u^{*,-}_{21}}{\left|u^{*}_{21}\right|} h_{21} f^{*}_{21}\left(w^{n}_{2,i-1}, w^{n}_{1,i}\right),$$

$$F^{Lag,1}_{i-1/2} = -\frac{u^{*,+}_{12}}{\left|u^{*}_{12}\right|} h_{12} f^{Lag*}_{12}\left(w^{n}_{1,i-1}, w^{n}_{2,i}\right) + \frac{u^{*,+}_{21}}{\left|u^{*}_{21}\right|} h_{21} f^{Lag,*}_{21}\left(w^{n}_{2,i-1}, w^{n}_{1,i}\right).$$

In these two formulas, it is clear that two-phase fluxes F are obtained as a sum of Euler equations fluxes f. For the sake of clarity, we have used the following functions,

$$\omega^{+} = \mathrm{Max}\left(0, \omega\right) = \frac{\omega + |\omega|}{2},\ \omega^{-} = \mathrm{Min}\left(0, \omega\right) = \frac{\omega - |\omega|}{2}.$$

3.2 Determination of the interfacial variables u_I and P_I

The determination of the interfacial variables u_I and P_I is based on the 2D topology with decoupled flow channels, as shown in Figure 1. The interfacial variables determination depends on the type of contact between the two phases: contact 1-2 or contact 2-1. It is determined by the sign of $(\alpha_{1L} - \alpha_{1R})$, as shown in Figure 2.

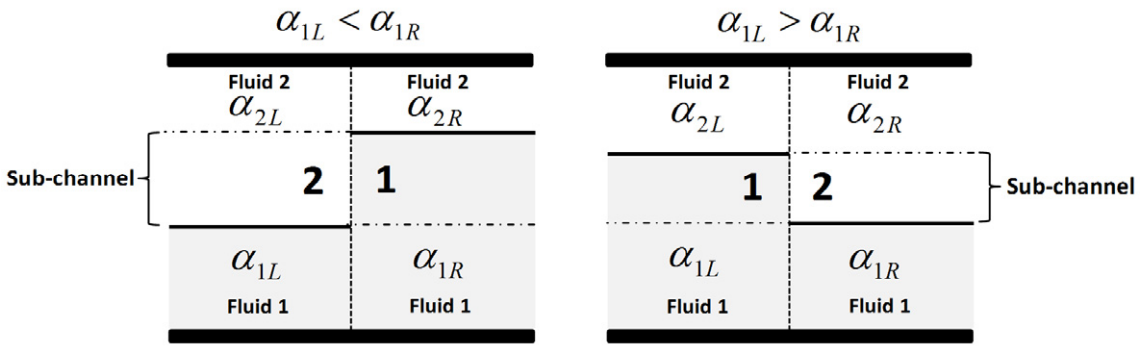

Figure 2: Schematic representation of the two types of contact that may appear at a given cell boundary.

The lower scripts L and R are relative respectively to the left and right states. For each contact the Riemann problem of the Euler equations with different fluids has to be solved. As the Riemann problem solution depends only of initial states L and R, variables u_I and P_I are locally constant during a time step at a given cell boundary. They are computed by an appropriate Riemann solver (exact or approximate) with correct initial states as inputs. The example of the HLLC Riemann solver for the Euler equations is used hereafter.

Contact 2-1

The corresponding (x,t) diagram in the HLLC solver frame is shown in Figure 3.

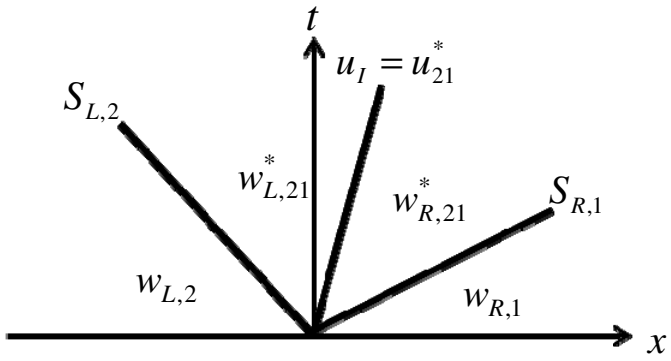

Figure 3: Wave pattern in the frame of the HLLC Riemann solver for contact 2-1. 'w' represents the set of variables of the Euler equations.

Contact 2-1 appears when $\alpha_{1L} < \alpha_{1R}$. The wave speeds $S_{L,2}$ and $S_{R,1}$ are estimated as:

$$S_{R,1} = \mathrm{Max}\left(u_{L,1} + c_{L,1}, u_{R,1} + c_{R,1}\right),$$

$$S_{L,2} = \mathrm{Min}\left(u_{L,2} - c_{L,2}, u_{R,2} - c_{R,2}\right).$$

The interfacial velocity and pressure are determined respectively under HLL and HLLC approximations as,

$$u_I = u_{21}^{*,\mathrm{HLL}} = \frac{\left(\rho u^2 + P\right)_{R,1} - \left(\rho u^2 + P\right)_{L,2} + S_{L,2}(\rho u)_{L,2} - S_{R,1}(\rho u)_{R,1}}{(\rho u)_{R,1} - (\rho u)_{L,2} + S_{L,2}\rho_{L,2} - S_{R,1}\rho_{R,1}},$$

$$P_I = P_{R,21}^{*} = \rho_{R,1}\left(u_{R,1} - S_{R,1}\right)\left(u_{R,1} - u_I\right) + P_{R,1}.$$

Contact 1-2

This contact corresponds to the symmetric situation when $\alpha_{1L} > \alpha_{1R}$. The corresponding wave pattern is shown in Figure 4.

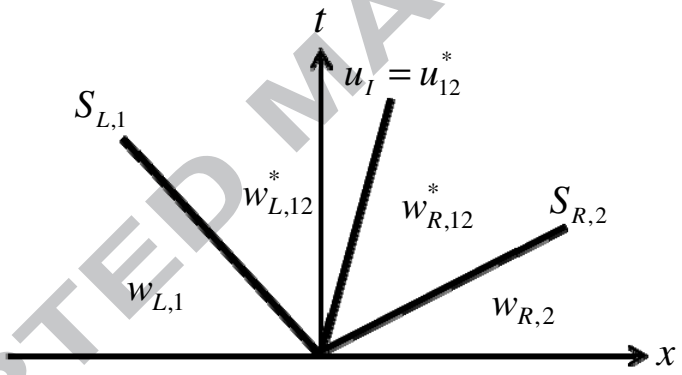

Figure 4: Wave pattern in the frame of the HLLC Riemann solver for contact 1-2.

The wave's speeds are now estimated as,

$$S_{R,2} = \mathrm{Max}\left(u_{L,2} + c_{L,2}, u_{R,2} + c_{R,2}\right),$$

$$S_{L,1} = \mathrm{Min}\left(u_{L,1} - c_{L,1}, u_{R,1} - c_{R,1}\right).$$

The interfacial variables are computed as,

$$u_I = u_{12}^{*,\mathrm{HLL}} = \frac{\left(\rho u^2 + P\right)_{R,2} - \left(\rho u^2 + P\right)_{L,1} + S_{L,1}(\rho u)_{L,1} - S_{R,2}(\rho u)_{R,2}}{(\rho u)_{R,2} - (\rho u)_{L,1} + S_{L,1}\rho_{L,1} - S_{R,2}\rho_{R,2}},$$

$$P_I = P_{R,12}^{*} = \rho_{R,2}\left(u_{R,2} - S_{R,2}\right)\left(u_{R,2} - u_I\right) + P_{R,2}.$$

Let us mention that the interfacial variables (2) and (3) that appear in the continuous system (1) result of similar computations, in the limit of weak amplitude waves.

In the former expressions of u_I and P_I, it is clear that these variables are constant at a given cell boundary and during a given time step. As these variables are local constants, System (4) expresses locally in conservative form:

$$\frac{\partial U_k}{\partial t}+\frac{\partial F_k}{\partial x}=0\,,\ \forall k\in\{1,2\} \tag{5}$$

with $U_k=\begin{pmatrix}\alpha_k\\(\alpha\rho)_k\\(\alpha\rho u)_k\\(\alpha\rho E)_k\end{pmatrix}$ and $F_k=\begin{pmatrix}\alpha_k u_I\\(\alpha\rho u)_k\\\alpha_k\left(\rho u^2+P\right)_k-\alpha_k P_I\\\alpha_k(\rho E+P)_k u_k-\alpha_k P_I u_I\end{pmatrix}$.

This remark simplifies significantly the two-phase Riemann problem resolution.

4. Two-phase Riemann solver

The two-phase flow model under consideration (1) is hyperbolic with 7 waves. For a given cell boundary, a HLLC type Riemann solver with 6 intermediate states is quite complex to manage. These difficulties increase with increasing number of fluids (3 and more).

The variables u_I and P_I being local constants, another important simplification appears. The Riemann problem for a given phase is decoupled to the one of the other phase. Thus, for a given phase k, the Riemann problem is based on the PDEs system (5) and on its own wave pattern as shown in Figure 5.

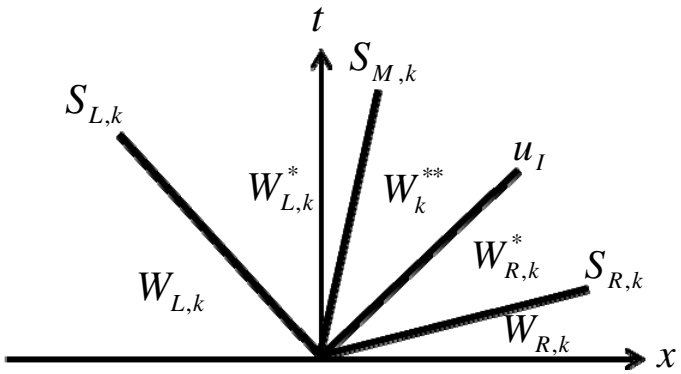

Figure 5: Schematic representation of the Riemann problem for a given phase k in the HLLC frame. 'W' represents the set of variables of the two-phase model.

In Figure 5, W_k denotes the vector of primitive variables of a given phase: $W_k = (\alpha_k, \quad \rho_k, \quad u_k, \quad P_k)^T$.

$W_{L,k}$ and $W_{R,k}$ are respectively the left and right initial states, known at each time step. The Rankine-Hugoniot relations across the various waves link the initial data to the intermediate states $W_{L,k}^*$, W_k^{**} and $W_{R,k}^*$

.

4.1 Wave speed estimates $S_{L,k}$, $S_{R,k}$ and $S_{M,k}$

The left- and right-facing wave speeds $S_{L,k}$ and $S_{R,k}$ are determined by the Davis (1988) estimates,

$$S_{R,k} = \text{Max}\left(u_{L,k} + c_{L,k}, u_{R,k} + c_{R,k}\right),$$

$$S_{L,k} = \text{Min}\left(u_{L,k} - c_{L,k}, u_{R,k} - c_{R,k}\right).$$

Let us mention that other wave speed estimates are possible. Denoting S_k^+ a positive wave speed for phase k, under Rusanov approximation it is possible to define $S_{R,k} = S_k^+$ and $S_{L,k} = -S_k^+$.

To estimate S_k^+, Davis (1988) considered the following guess:

$$S_k^+ = \text{Max}\left(\left|u_{L,k} - c_{L,k}\right|, \left|u_{R,k} - c_{R,k}\right|, \left|u_{L,k} + c_{L,k}\right|, \left|u_{R,k} + c_{R,k}\right|\right).$$

Toro (2009) recommanded the following one:

$$S_k^+ = \text{Max}\left(\left|u_{L,k}\right| + c_{L,k}, \left|u_{R,k}\right| + c_{R,k}\right).$$

WIth these wave speeds the intermediate contact wave is estimated under HLL (Harten et al., 1983) approximation as,

$$S_{M,k} = \frac{\alpha_{R,k}\left(\rho u^2 + P\right)_{R,k} - \alpha_{L,k}\left(\rho u^2 + P\right)_{L,k} + S_{L,k}(\alpha\rho u)_{L,k} - S_{R,k}(\alpha\rho u)_{R,k} + (\alpha_{L,k} - \alpha_{R,k})P_I}{(\alpha\rho u)_{R,k} - (\alpha\rho u)_{L,k} + S_{L,k}(\alpha\rho)_{L,k} - S_{R,k}(\alpha\rho)_{R,k}} \quad , \tag{6}$$

where u_I and P_I are already computed.

4.2 Determination of the intermediate states

In the following, two configurations are considered, as shown in Figure 6:

a) $\boxed{S_{L,k} < S_{M,k} < u_I < S_{R,k}}$ **b)** $\boxed{S_{L,k} < u_I < S_{M,k} < S_{R,k}}$

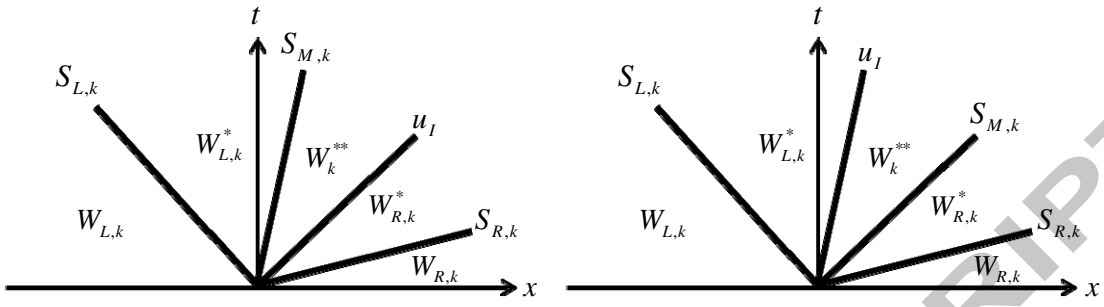

Figure 6: The two main wave configurations considered for the two-phase Riemann problem resolution.

The extreme situations $u_I > S_{R,k}$ and $u_I < S_{L,k}$ will be addressed latter.

In this section, the configuration **a)** only is considered: $S_{L,k} < S_{M,k} < u_I < S_{R,k}$. Configuration **b)** is addressed in Appendix A.

Across each wave, the Rankine-Hugoniot (RH) relations of System (5) read,

$$\begin{aligned}
F^*_{L,k} &= F_{L,k} + S_{L,k}\left(U^*_{L,k} - U_{L,k}\right),\\
F^*_{R,k} &= F_{R,k} + S_{R,k}\left(U^*_{R,k} - U_{R,k}\right),\\
F^{**}_k &= F^*_{R,k} + u_I\left(U^{**}_k - U^*_{R,k}\right),\\
F^*_{L,k} &= F^{**}_k + S_{M,k}\left(U^*_{L,k} - U^{**}_k\right).
\end{aligned} \tag{7}$$

To compute the flux in each intermediate state, the conservative variable vectors $U^*_{L,k}$, $U^*_{R,k}$ and U^{**}_k are needed.

Across the contact wave the RH relations reduce to:

$$u^*_{L,k} = u^{**}_k = S_{M,k} \tag{8}$$

$$P^*_{L,k} = P^{**}_k \tag{9}$$

As the interface velocity u_I is a local constant at a given cell boundary the volume fraction equation expresses in local conservation form. It has the following jumps,

$\alpha^*_{L,k} = \alpha^{**}_k = \alpha_{L,k}$,

$\alpha^*_{R,k} = \alpha_{R,k}$,

that are in perfect agreement with the non-conservative formulation of the volume fraction equation.

State $W^*_{L,k}$

This state is readily obtained from the wave speed estimates and knowledge of the left state:

$$\alpha^*_{L,k} = \alpha_{L,k},$$

$$\rho^*_{L,k} = \rho_{L,k}\frac{u_{L,k} - S_{L,k}}{S_{M,k} - S_{L,k}},$$

$$u^*_{L,k} = S_{M,k},$$

$$P^*_{L,k} = P_{L,k} + \rho_{L,k}\left(u_{L,k} - S_{L,k}\right)\left(u_{L,k} - S_{M,k}\right), \tag{10}$$

$$E^*_{L,k} = E_{L,k} + \frac{(Pu)_{L,k} - P^*_{L,k}S_{M,k}}{\rho_{L,k}\left(u_{L,k} - S_{L,k}\right)}.$$

State $W^*_{R,k}$

The main difficulty relies in the determination of $u^*_{R,k}$. To do this mass and momentum jump relations (7) across $S_{R,k}$, u_I, $S_{M,k}$ and $S_{L,k}$ are considered. Let's start with jump relations across $S_{R,k}$ and u_I :

$$\alpha_{L,k}\rho^{**}_k\left(u^{**}_k - u_I\right) = \alpha_{R,k}\rho^*_{R,k}\left(u^*_{R,k} - u_I\right) \tag{11}$$

$$\alpha_{L,k}\rho^{**}_k u^{**}_k\left(u^{**}_k - u_I\right) + \alpha_{L,k}P^{**}_k = \alpha_{R,k}\rho^*_{R,k}u^*_{R,k}\left(u^*_{R,k} - u_I\right) + \alpha_{R,k}P^*_{R,k} + \left(\alpha_{L,k} - \alpha_{R,k}\right)P_I \tag{12}$$

$$\rho^*_{R,k}\left(u^*_{R,k} - S_{R,k}\right) = \rho_{R,k}\left(u_{R,k} - S_{R,k}\right) \tag{13}$$

$$\rho^*_{R,k}u^*_{R,k}\left(u^*_{R,k} - S_{R,k}\right) + P^*_{R,k} = \rho_{R,k}u_{R,k}\left(u_{R,k} - S_{R,k}\right) + P_{R,k} \tag{14}$$

Combining (13) with (14) provides an expression for $P^*_{R,k}$:

$$P^*_{R,k} = \rho_{R,k}\left(u_{R,k} - S_{R,k}\right)\left(u_{R,k} - u^*_{R,k}\right) + P_{R,k}$$

Inserting (11) in (12) and using (8) and (9) imply:

$$\alpha_{R,k}\rho^*_{R,k}\left(u^*_{R,k}-u_I\right)\left(S_{M,k}-u^*_{R,k}\right)=\alpha_{R,k}P^*_{R,k}-\alpha_{L,k}P^*_{L,k}+\left(\alpha_{L,k}-\alpha_{R,k}\right)P_I$$

Inserting the expression for $P^*_{R,k}$ in this equation yields,

$$\alpha_{R,k}\rho_{R,k}\left(u_{R,k}-S_{R,k}\right)\left(\frac{\left(u^*_{R,k}-u_I\right)\left(S_{M,k}-u^*_{R,k}\right)}{\left(u^*_{R,k}-S_{R,k}\right)}-\left(u_{R,k}-u^*_{R,k}\right)\right)=\alpha_{R,k}P_{R,k}-\alpha_{L,k}P^*_{L,k}+\left(\alpha_{L,k}-\alpha_{R,k}\right)P_I.$$

After rearrangement, the expression for $u^*_{R,k}$ is obtained:

$$u^*_{R,k}=\frac{\left((\alpha P)_{R,k}-(\alpha P)^*_{L,k}+\left(\alpha_{L,k}-\alpha_{R,k}\right)P_I\right)S_{R,k}-(\alpha\rho)_{R,k}\left(u_{R,k}-S_{R,k}\right)\left(u_IS_{M,k}-S_{R,k}u_{R,k}\right)}{(\alpha\rho)_{R,k}\left(u_{R,k}-S_{R,k}\right)\left(S_{R,k}-u_I-S_{M,k}+u_{R,k}\right)+(\alpha P)_{R,k}-(\alpha P)^*_{L,k}+\left(\alpha_{L,k}-\alpha_{R,k}\right)P_I} \quad (15)$$

This expression can be significantly simplified by inserting $P^*_{L,k}$ given by Equation (10). After tedious calculations the following result is obtained:

$$u^*_{R,k}=S_{M,k} \quad (16)$$

Consequently, all intermediate material velocities are equal:

$$u^*_{L,k}=u^{**}_k=u^*_{R,k}=S_{M,k} \quad (17)$$

This unexpected result will be shown to be in agreement with the second law of thermodynamics.

Relation (17) is a consequence of the weak form of System (5) (HLL-type approximation) that provides the intermediate flow speed, that already accounts for the interactions with the other phase through the non-conservative terms.

The $W^*_{R,k}$ state is then readily obtained,

$$\alpha^*_{R,k}=\alpha_{R,k},$$

$$\rho^*_{R,k}=\rho_{R,k}\frac{u_{R,k}-S_{R,k}}{S_{M,k}-S_{R,k}},$$

$$u^*_{R,k}=S_{M,k},$$

$$P^*_{R,k}=P_{R,k}+\rho_{R,k}\left(u_{R,k}-S_{R,k}\right)\left(u_{R,k}-S_{M,k}\right),$$

$$E^*_{R,k}=E_{R,k}+\frac{(Pu)_{R,k}-P^*_{R,k}S_{M,k}}{\rho_{R,k}\left(u_{R,k}-S_{R,k}\right)}.$$

State W_k^{**}

The invariance of the material velocity in the various intermediate states implies continuity of the variable $(\alpha\rho)_k$ across wave u_I :

$$(\alpha\rho)_k^{**} = (\alpha\rho)_{R,k}^{*} .$$

Moreover, the pressure in state W_k^{**} is given by,

$$P_k^{**} = P_{L,k}^{*} . \tag{18}$$

It can also be expressed by the momentum jump relation across wave u_I ,

$$P_k^{**} = \frac{\alpha_{R,k}}{\alpha_{L,k}} P_{R,k}^{*} + \frac{\alpha_{L,k} - \alpha_{R,k}}{\alpha_{L,k}} P_I . \tag{19}$$

This last expression is used hereafter to express the total energy,

$$E_k^{**} = E_{R,k}^{*} - \frac{\alpha_{L,k} - \alpha_{R,k}}{(\alpha\rho)_{R,k}^{*}} P_I . \tag{20}$$

4.3 Summary

We now have in hands the three intermediate states conservative variable vectors,

$$U_{L,k}^{*} = \begin{pmatrix} \alpha_{L,k} \\ (\alpha\rho)_{L,k}^{*} \\ (\alpha\rho)_{L,k}^{*} S_{M,k} \\ (\alpha\rho)_{L,k}^{*} E_{L,k}^{*} \end{pmatrix}, \; U_{R,k}^{*} = \begin{pmatrix} \alpha_{R,k} \\ (\alpha\rho)_{R,k}^{*} \\ (\alpha\rho)_{R,k}^{*} S_{M,k} \\ (\alpha\rho)_{R,k}^{*} E_{R,k}^{*} \end{pmatrix} \text{ and } U_k^{**} = \begin{pmatrix} \alpha_{L,k} \\ (\alpha\rho)_k^{**} \\ (\alpha\rho)_k^{**} S_{M,k} \\ (\alpha\rho)_k^{**} E_k^{**} \end{pmatrix},$$

with,

$$S_{M,k} = \frac{\alpha_{R,k}(\rho u^2 + P)_{R,k} - \alpha_{L,k}(\rho u^2 + P)_{L,k} + S_{L,k}(\alpha\rho u)_{L,k} - S_{R,k}(\alpha\rho u)_{R,k} + (\alpha_{L,k} - \alpha_{R,k})P_I}{(\alpha\rho u)_{R,k} - (\alpha\rho u)_{L,k} + S_{L,k}(\alpha\rho)_{L,k} - S_{R,k}(\alpha\rho)_{R,k}} .$$

State $W_{L,k}^{*}$

$$\alpha_{L,k}^{*} = \alpha_{L,k} ; \qquad \rho_{L,k}^{*} = \rho_{L,k} \frac{u_{L,k} - S_{L,k}}{S_{M,k} - S_{L,k}} ; \qquad u_{L,k}^{*} = S_{M,k} ;$$

$$P_{L,k}^{*} = P_{L,k} + \rho_{L,k}(u_{L,k} - S_{L,k})(u_{L,k} - S_{M,k}) ; \qquad E_{L,k}^{*} = E_{L,k} + \frac{(Pu)_{L,k} - P_{L,k}^{*} S_{M,k}}{\rho_{L,k}(u_{L,k} - S_{L,k})} .$$

- **State** $W^{*}_{R,k}$

$$\alpha^{*}_{R,k} = \alpha_{R,k} \; ; \quad \rho^{*}_{R,k} = \rho_{R,k}\frac{u_{R,k} - S_{R,k}}{S_{M,k} - S_{R,k}}; \qquad u^{*}_{R,k} = S_{M,k} \; ;$$

$$P^{*}_{R,k} = P_{R,k} + \rho_{R,k}\left(u_{R,k} - S_{R,k}\right)\left(u_{R,k} - S_{M,k}\right); \qquad E^{*}_{R,k} = E_{R,k} + \frac{(Pu)_{R,k} - P^{*}_{R,k}S_{M,k}}{\rho_{R,k}\left(u_{R,k} - S_{R,k}\right)} \; .$$

- **State** W^{**}_{k}

$$\alpha^{**}_{k} = \alpha_{L,k} \; ; \qquad (\alpha\rho)^{**}_{k} = (\alpha\rho)^{*}_{R,k} \; ; \qquad u^{**}_{k} = S_{M,k} \; ;$$

$$P^{**}_{k} = P^{*}_{L,k} \; ; \qquad E^{**}_{k} = E^{*}_{R,k} - \frac{\alpha_{L,k} - \alpha_{R,k}}{(\alpha\rho)^{*}_{R,k}} P_I \; .$$

The fluxes in the various intermediate states are deduced from (7).

4.4 Solution sampling

Let us recall that two wave patterns are possible,

- $S_{L,k} < S_{M,k} < u_I < S_{R,k}$,
- $S_{L,k} < u_I < S_{M,k} < S_{R,k}$.

In the cases of very high drift velocity among the phases, it is possible that u_I be outside the range $]S_{L,k}, S_{R,k}[$ of a given phase. To avoid this issue the following strategy has been adopted. If u_I exceeds 90% of the wave velocity $S_{R,k}$, then $S_{R,k}$ is reset to the maximum wave speed of all phases,

$$S_{R,k} := \underset{k}{\mathrm{Max}}\left(S_{R,k}\right).$$

The same is done for the left facing wave speed,

$$S_{L,k} := \underset{k}{\mathrm{Min}}\left(S_{L,k}\right).$$

With the help of the intermediate states and fluxes summarized in Section 4.3 the last step consists in the solution sampling,

$$\text{if } S_{M,k} < u_I \text{, then } F_k^* = \begin{cases} F_{L,k} & \text{if } S_{L,k} \geq 0 \\ F_{L,k}^* & \text{if } S_{L,k} < 0 \text{ and } S_{M,k} \geq 0 \\ F_k^{**} & \text{if } S_{M,k} < 0 \text{ and } u_I > 0 \\ F_{R,k}^* & \text{if } u_I \leq 0 \text{ and } S_{R,k} > 0 \\ F_{R,k} & \text{if } S_{R,k} \leq 0 \end{cases},$$

$$\text{if } u_I < S_{M,k} \text{, then } F_k^* = \begin{cases} F_{L,k} & \text{if } S_{L,k} \geq 0 \\ F_{L,k}^* & \text{if } S_{L,k} < 0 \text{ and } u_I \geq 0 \\ F_k^{**} & \text{if } u_I < 0 \text{ and } S_{M,k} > 0 \\ F_{R,k}^* & \text{if } S_{M,k} \leq 0 \text{ and } S_{R,k} > 0 \\ F_{R,k} & \text{if } S_{R,k} \leq 0 \end{cases}.$$

We now check solver's agreement with the second law of thermodynamics.

5. Entropy preserving

Robustness of the solver is related to densities and volume fractions positivity as well as agreement with the second law of thermodynamics. These properties are matched by the HLLC solver for the Euler equations (Bouchut, 2004). We examine entropy production of the solver in the present two-phase context, for the wave configuration $S_{M,k} < u_I$ considered previously.

Waves speeds $S_{L,k}$ and $S_{R,k}$ are considered as single phase shocks in phase k. The single phase analysis and results of Bouchut (2004) are therefore still valid, showing agreement with the second law of thermodynamics across these waves. However, a fourth wave (u_I) appears in the two-phase context and it is necessary to show that the entropy production is positive across this wave, separating states $W_{R,k}^*$ and W_k^{**}. There is no evidence, as it has been shown previously that the material velocity is constant across this wave, a non intuitive fact.

Expanding the energy jump relation (20) the following result is obtained,

$$e_k^{**} + \frac{1}{2} u_k^{**2} = e_{R,k}^* + \frac{1}{2} u_{R,k}^{*\,2} - \frac{\alpha_{L,k} - \alpha_{R,k}}{(\alpha\rho)_{R,k}^*} P_I .$$

The invariance of the material velocity in these two states implies,

$$e_k^{**} = e_{R,k}^{*} - \frac{\alpha_{L,k} - \alpha_{R,k}}{(\alpha\rho)_{R,k}^{*}} P_I . \tag{21}$$

The Gibbs identity of a given phase reads,

$$de_k = T_k d\tau_k - P_k dv_k$$

with τ_k and $v_k = \frac{1}{\rho_k}$ representing respectively the entropy and the specific volume of phase k.

The Gibbs relation expressed across wave u_I thus reads,

$$\overline{T}_k \left(\eta_k^{**} - \eta_{R,k}^{*}\right) = e_k^{**} - e_{R,k}^{*} + \overline{P}_k \left(v_k^{**} - v_{R,k}^{*}\right),$$

where $\overline{T}_k$ and $\overline{P}_k$ represent respectively temperature and pressure averages.

With the help of (21) and mass jump condition expressed as,

$$v_k^{**} = \frac{\alpha_{L,k}}{\alpha_{R,k}} v_{R,k}^{*},$$

the discrete Gibbs identity becomes,

$$\overline{T}_k \left(\eta_k^{**} - \eta_{R,k}^{*}\right) = \left(\overline{P}_k - P_I\right)\left(\frac{\alpha_{L,k}}{\alpha_{R,k}} - 1\right) v_{R,k}^{*} . \tag{22}$$

As $\overline{T}_k$ is obviously positive, it is necessary to show that the right hand side of (22) is positive too.

For weak enough discontinuities it is reasonable to assume,

$$\overline{P}_k = \frac{1}{2}\left(P_k^{**} + P_{R,k}^{*}\right). \tag{23}$$

Inserting (23) and (19) in (22) the entropy jump now reads,

$$\overline{T}_k \left(\eta_k^{**} - \eta_{R,k}^{*}\right) = \frac{1}{2}\left(P_{R,k}^{*} - P_I\right)\left(\frac{\alpha_{L,k}}{\alpha_{R,k}} - \frac{\alpha_{R,k}}{\alpha_{L,k}}\right) v_{R,k}^{*} .$$

Let us now specify the calculations to phase 1:

$$T_1 \left(\eta_1^{**} - \eta_{R,1}^{*}\right) = \frac{1}{2}\left(P_{R,1}^{*} - P_I\right)\left(\frac{\alpha_{L,1}}{\alpha_{R,1}} - \frac{\alpha_{R,1}}{\alpha_{L,1}}\right) v_{R,1}^{*} .$$

Two instances have to be considered.

Configuration $\alpha_{L,1} < \alpha_{R,1}$

In this situation, necessarily,

$$\left(\frac{\alpha_{L,1}}{\alpha_{R,1}} - \frac{\alpha_{R,1}}{\alpha_{L,1}}\right) < 0 .$$

Moreover, when $\alpha_{L,1} < \alpha_{R,1}$, the interface corresponds to a contact 2-1 and the expression for P_I, as given in Section 3.2 reads,

$$P_I = P^*_{R,21} = \rho_{R,1}\left(u_{R,1} - S_{R,1}\right)\left(u_{R,1} - u_I\right) + P_{R,1}.$$

Therefore,

$$P^*_{R,1} - P_I = \rho_{R,1}\left(u_{R,1} - S_{R,1}\right)\left(u_I - S_{M,1}\right).$$

This term is negative as $u_{R,1} - S_{R,1} < 0$ and $u_I - S_{M,1} > 0$. The entropy production is consequently positive.

Configuration $\alpha_{L,1} > \alpha_{R,1}$

It implies,

$$\left(\frac{\alpha_{L,1}}{\alpha_{R,1}} - \frac{\alpha_{R,1}}{\alpha_{L,1}}\right) > 0 .$$

This situation ($\alpha_{L,1} > \alpha_{R,1}$) corresponds to a contact 1-2 with $P_I = P^*_{L,12} = P^*_{R,12}$ given by:

$$P_I = P^*_{L,12} = \rho_{L,1}\left(u_{L,1} - S_{L,1}\right)\left(u_{L,1} - u_I\right) + P_{L,1}$$

With the help of Relations (10), (18) and (19) it is possible to express $P^*_{R,1}$ as a function of $P_{L,1}$ and P_I,

$$P^*_{R,1} = \frac{\alpha_{L,1}}{\alpha_{R,1}}\left(P_{L,1} + \rho_{L,1}\left(u_{L,1} - S_{L,1}\right)\left(u_{L,1} - S_{M,1}\right)\right) - \left(\frac{\alpha_{L,1}}{\alpha_{R,1}} - 1\right)P_I .$$

Consequently,

$$P^*_{R,1} - P_I = \frac{\alpha_{L,1}}{\alpha_{R,1}}\rho_{L,1}\left(u_{L,1} - S_{L,1}\right)\left(u_I - S_{M,1}\right).$$

This term is positive as $u_{L,l} - S_{L,l} > 0$ and $u_I - S_{M,l} > 0$. The entropy production across wave u_I is therefore positive. There is no difficulty to make the same proof for phase 2.

Computational experiments of Section 7 illustrate the entropy preserving character of the present solver.

6. Godunov type scheme

Having the HLLC two-phase Riemann solver in hands, it is now possible to derive a Godunov type scheme. For the sake of simplicity, the first-order version only is presented, its higher order variant being given in Appendix B.

As the entire cell is now considered, it is not possible to consider local conservative formulation. The system is thus considered under the form (4),

$$\frac{\partial U_k}{\partial t} + \frac{\partial F_k}{\partial x} + \alpha_k \frac{\partial H_k}{\partial x} = 0, \ \forall k \in \{1,2\}, \tag{24}$$

with $U_k = \begin{pmatrix} \alpha_k \\ (\alpha\rho)_k \\ (\alpha\rho u)_k \\ (\alpha\rho E)_k \end{pmatrix}$, $F_k = \begin{pmatrix} \alpha_k u_I \\ (\alpha\rho u)_k \\ \alpha_k (\rho u^2 + P)_k - \alpha_k P_I \\ \alpha_k (\rho E + P)_k u_k - \alpha_k P_I u_I \end{pmatrix}$ and $H_k = \begin{pmatrix} -u_I \\ 0 \\ P_I \\ P_I u_I \end{pmatrix}$.

For a given cell i, the Godunov scheme we consider reads,

$$U_{k,i}^{n+1} = U_{k,i}^{n} - \frac{\Delta t}{\Delta x}\left[F_{k,i+\frac{1}{2}}^{*} - F_{k,i-\frac{1}{2}}^{*} + \alpha_{k,i}^{n}\left(H_{k,i+\frac{1}{2}}^{*} - H_{k,i-\frac{1}{2}}^{*}\right)\right], \ \forall k \in \{1,2\},$$

with $H_{k,i\pm\frac{1}{2}}^{*} = \left(-(u_I)_{k,i\pm\frac{1}{2}}, \quad 0, \quad (P_I)_{k,i\pm\frac{1}{2}}, \quad (P_I u_I)_{k,i\pm\frac{1}{2}}\right)^T$.

Δx and Δt represent respectively the space and time step. The superscripts n and $n+1$ denote two successive time steps t^n and t^{n+1}.

This method is stable under conventional CFL restriction:

$$\Delta t = CFL \frac{\Delta x}{Max\left(S_{L,k}, S_{R,k}\right)}.$$

In the above Godunov type scheme, the non-conservative terms have been approximated with the simplest method. Let us examine this approximation more deeply.

Non-conservative terms

Let us focus on the term $\alpha_k \frac{\partial H_k}{\partial x}$ and justify its discrete form as $\alpha_{k,i}^n \left(H_{k,i+\frac{1}{2}}^* - H_{k,i-\frac{1}{2}}^* \right) / \Delta x$ at least with respect to the DEM.

In the DEM framework the discrete form of the non-conservative term $H_k \frac{\partial \alpha_k}{\partial x}$ corresponds to $\frac{F_{i+1/2}^{Lag,k} + F_{i-1/2}^{Lag,k}}{\Delta x}$ appearing in the numerical scheme given in Section 3.1 and representing the Lagrangian fluxes contribution.

Assuming regular enough functions, we have,

$$H_k \frac{\partial \alpha_k}{\partial x} = \frac{\partial \alpha_k H_k}{\partial x} - \alpha_k \frac{\partial H_k}{\partial x}.$$

With the following discrete analog,

$$\frac{(\alpha H)_{k,i+\frac{1}{2}}^* - (\alpha H)_{k,i-\frac{1}{2}}^*}{\Delta x} - \alpha_{k,i}^n \frac{\left(H_{k,i+\frac{1}{2}}^* - H_{k,i-\frac{1}{2}}^* \right)}{\Delta x},$$

the formulation appearing in (24) is recovered.

To show agreement with the DEM it is necessary to show that,

$$(\alpha H)_{k,i+\frac{1}{2}}^* - (\alpha H)_{k,i-\frac{1}{2}}^* - \alpha_{k,i}^n \left(H_{k,i+\frac{1}{2}}^* - H_{k,i-\frac{1}{2}}^* \right) = F_{i+1/2}^{Lag,k} + F_{i-1/2}^{Lag,k}.$$

Let us now specify the calculations for phase 1.

On the one hand, we have:

$$\begin{aligned} &(\alpha H)_{1,i+\frac{1}{2}}^* - (\alpha H)_{1,i-\frac{1}{2}}^* - \alpha_{1,i}^n \left(H_{1,i+\frac{1}{2}}^* - H_{1,i-\frac{1}{2}}^* \right) \\ &= \left(\alpha_{1,i+\frac{1}{2}}^* - \alpha_{1,i}^n \right) H_{1,i+\frac{1}{2}}^* + \left(\alpha_{1,i}^n - \alpha_{1,i-\frac{1}{2}}^* \right) H_{1,i-\frac{1}{2}}^* \\ &= \left(\alpha_{1,i}^n \left(\frac{u_I^+}{|u_I|} \right)_{i+1/2} - \alpha_{1,i+1}^n \left(\frac{u_I^-}{|u_I|} \right)_{i+1/2} - \alpha_{1,i}^n \right) H_{1,i+\frac{1}{2}}^* + \left(\alpha_{1,i}^n - \alpha_{1,i-1}^n \left(\frac{u_I^+}{|u_I|} \right)_{i-1/2} + \alpha_{1,i}^n \left(\frac{u_I^-}{|u_I|} \right)_{i-1/2} \right) H_{1,i-\frac{1}{2}}^* \end{aligned} \quad (25)$$

On the other hand we have,

$$F^{Lag,l}_{i+1/2}+F^{Lag,l}_{i-1/2}=\left(\frac{u^{*,-}_{12}}{|u^{*}_{12}|}h_{12}\right)_{i+1/2} f^{Lag^*}_{12}\left(w^{n}_{1,i},w^{n}_{2,i+1}\right)-\left(\frac{u^{*,-}_{21}}{|u^{*}_{21}|}h_{21}\right)_{i+1/2} f^{Lag,*}_{21}\left(w^{n}_{2,i},w^{n}_{1,i+1}\right)$$
$$-\left(\frac{u^{*,+}_{12}}{|u^{*}_{12}|}h_{12}\right)_{i-1/2} f^{Lag^*}_{12}\left(w^{n}_{1,i-1},w^{n}_{2,i}\right)+\left(\frac{u^{*,+}_{21}}{|u^{*}_{21}|}h_{21}\right)_{i-1/2} f^{Lag,*}_{21}\left(w^{n}_{2,i-1},w^{n}_{1,i}\right) \quad (26)$$

Inserting the heights h_{12} and h_{21} definitions,

$$F^{Lag,l}_{i+1/2}+F^{Lag,l}_{i-1/2}=\left(\frac{u^{*,-}_{12}}{|u^{*}_{12}|}\right)_{i+1/2} Max\left(0,\alpha^{n}_{1,i}-\alpha^{n}_{1,i+1}\right)f^{Lag^*}_{12}\left(w^{n}_{1,i},w^{n}_{2,i+1}\right)-\left(\frac{u^{*,-}_{21}}{|u^{*}_{21}|}\right)_{i+1/2} Max\left(0,\alpha^{n}_{1,i+1}-\alpha^{n}_{1,i}\right)f^{Lag,*}_{21}\left(w^{n}_{2,i},w^{n}_{1,i+1}\right)$$
$$-\left(\frac{u^{*,+}_{12}}{|u^{*}_{12}|}\right)_{i-1/2} Max\left(0,\alpha^{n}_{1,i-1}-\alpha^{n}_{1,i}\right)f^{Lag^*}_{12}\left(w^{n}_{1,i-1},w^{n}_{2,i}\right)+\left(\frac{u^{*,+}_{21}}{|u^{*}_{21}|}\right)_{i-1/2} Max\left(0,\alpha^{n}_{1,i}-\alpha^{n}_{1,i-1}\right)f^{Lag,*}_{21}\left(w^{n}_{2,i-1},w^{n}_{1,i}\right)$$

Let's consider the example of positive velocity flow at both cell boundaries. The latter expression reduces to,

$$F^{Lag,l}_{i+1/2}+F^{Lag,l}_{i-1/2}=Max\left(0,\alpha^{n}_{1,i}-\alpha^{n}_{1,i-1}\right)f^{Lag,*}_{21}\left(w^{n}_{2,i-1},w^{n}_{1,i}\right)-Max\left(0,\alpha^{n}_{1,i-1}-\alpha^{n}_{1,i}\right)f^{Lag^*}_{12}\left(w^{n}_{1,i-1},w^{n}_{2,i}\right).$$

Let's now assume a monotonic decreasing volume fraction profile,

$$\alpha^{n}_{1,i-1}>\alpha^{n}_{1,i}>\alpha^{n}_{1,i+1}.$$

Therefore,

$$F^{Lag,l}_{i+1/2}+F^{Lag,l}_{i-1/2}=\left(\alpha^{n}_{1,i}-\alpha^{n}_{1,i-1}\right)f^{Lag^*}_{12}\left(w^{n}_{1,i-1},w^{n}_{2,i}\right).$$

Let's now consider (25). In the same flow conditions of positive velocity and decreasing volume fraction it reduces to,

$$(\alpha H)^{*}_{1,i+\frac{1}{2}}-(\alpha H)^{*}_{1,i-\frac{1}{2}}-\alpha^{n}_{1,i}\left(H^{*}_{1,i+\frac{1}{2}}-H^{*}_{1,i-\frac{1}{2}}\right)=\left(\alpha^{n}_{1,i}-\alpha^{n}_{1,i-1}\right)H^{*}_{1,i-\frac{1}{2}}.$$

In the present context, the only fluids contact to consider is contact 1-2. In this situation,

$$H^{*}_{1,i-\frac{1}{2}}=f^{Lag^*}_{12}\left(w^{n}_{1,i-1},w^{n}_{2,i}\right).$$

This example shows agreement between the discrete form $\alpha^{n}_{k,i}\left(H^{*}_{k,i+\frac{1}{2}}-H^{*}_{k,i-\frac{1}{2}}\right)$ and the DEM one.

The other flow configurations are examined in Appendix E showing perfect agreement with the DEM in all instances.

Relaxation solvers

Source and relaxation terms have been omitted from Section 3 with the quest of an appropriate hyperbolic solver. However, relaxation effects may be of paramount importance in multiphase mixtures. Stiff mechanical relaxation effects may also be used to solve interfacial flows, in order to fulfil interface conditions of equal pressures and equal normal velocities (Saurel and Abgrall, 1999). Corresponding stiff solvers are summarized in Appendix C and D.

7. Computational examples and validations

The method is validated on a series of test problems involving both velocity disequilibrium and stiff mechanical equilibrium, such as different two-phase shock tube test problems, a sedimentation test, and the Rogue et al. (1998) two-phase test. When available, exact solutions are used as well as experimental data. Comparison with the DEM is also addressed. Three-dimensional computations are also presented at the end of this section to illustrate method's capabilities.

In all tests that follow, the materials are assumed governed by the 'stiffened-gas' (SG) equation of state (EOS):

$$P_k = (\gamma_k - 1)\rho_k e_k - \gamma_k P_{\infty,k} \text{ , with } k \in \{g,l\} \tag{27}$$

This EOS involves both molecular thermal agitation through the term $(\gamma_k - 1)\rho_k e_k$ and attractive short distance intermolecular effects through the term $-\gamma_k P_{\infty,k}$. These attractive effects are present only in condensed materials.

Parameters for the gas phase are $\gamma_g = 1.4$ and $P_{\infty,g} = 0\,\text{Pa}$ while for the liquid phase they are $\gamma_l = 4.4$ and $P_{\infty,l} = 6\times 10^8\,\text{Pa}$. Obviously, other convex EOS can be used, see for example Chinnayya et al. (2004).

The entropy definition associated to (27) reads,

$$\eta_k = c_{v,k} \ln\left(\frac{P_k + P_{\infty,k}}{\rho_k^{\gamma_k}}\right) + q_k ,$$

where $c_{v,k}$ represents the specific heat at constant volume of phase k and q_k the entropy of formation.

As both $c_{v,k}$ and q_k are constants, the evolution of $(P_k + P_{\infty,k})/\rho_k{}^{\gamma_k}$ provides the qualitative behaviour of the entropies. This variable will be used to check the entropy preserving character of the method.

In the following, velocity non-equilibrium two-phase flows are addressed first. Method capabilities to deal with single velocity flows with the help of stiff relaxation solvers are addressed secondly.

All 1D tests shown hereafter are achieved with $\mathrm{CFL} = 0.8$.

7.1 Velocity disequilibrium two-phase flow tests

Two-phase shock tube without relaxation effects

The shock tube contains two-separated fluids with uniform volume fraction ($\alpha_g = 0.5$) everywhere. The left chamber has the same high pressure for both phases (10^9 Pa) while the right one has the same low pressure (10^5 Pa) for both phases. Gas and liquid densities are respectively set to $50\ \mathrm{kg/m^3}$ and $1000\ \mathrm{kg/m^3}$.

No source, no relaxation terms are used in this run, making the phases evolutions fully decoupled. Results are shown in Figure 7 at time $79\ \mu\mathrm{s}$. The second order variant of the method is used, with Van Leer limiter. The numerical solution is compared to the exact one, showing excellent agreement. This test is done with a uniform mesh involving 200 cells.

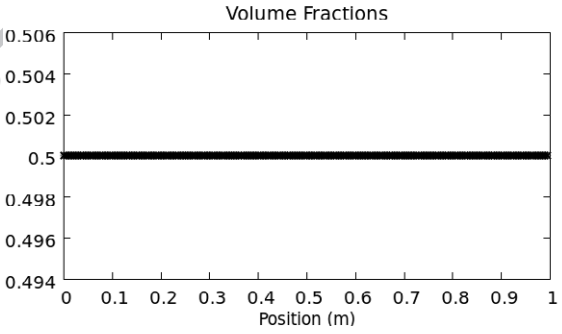

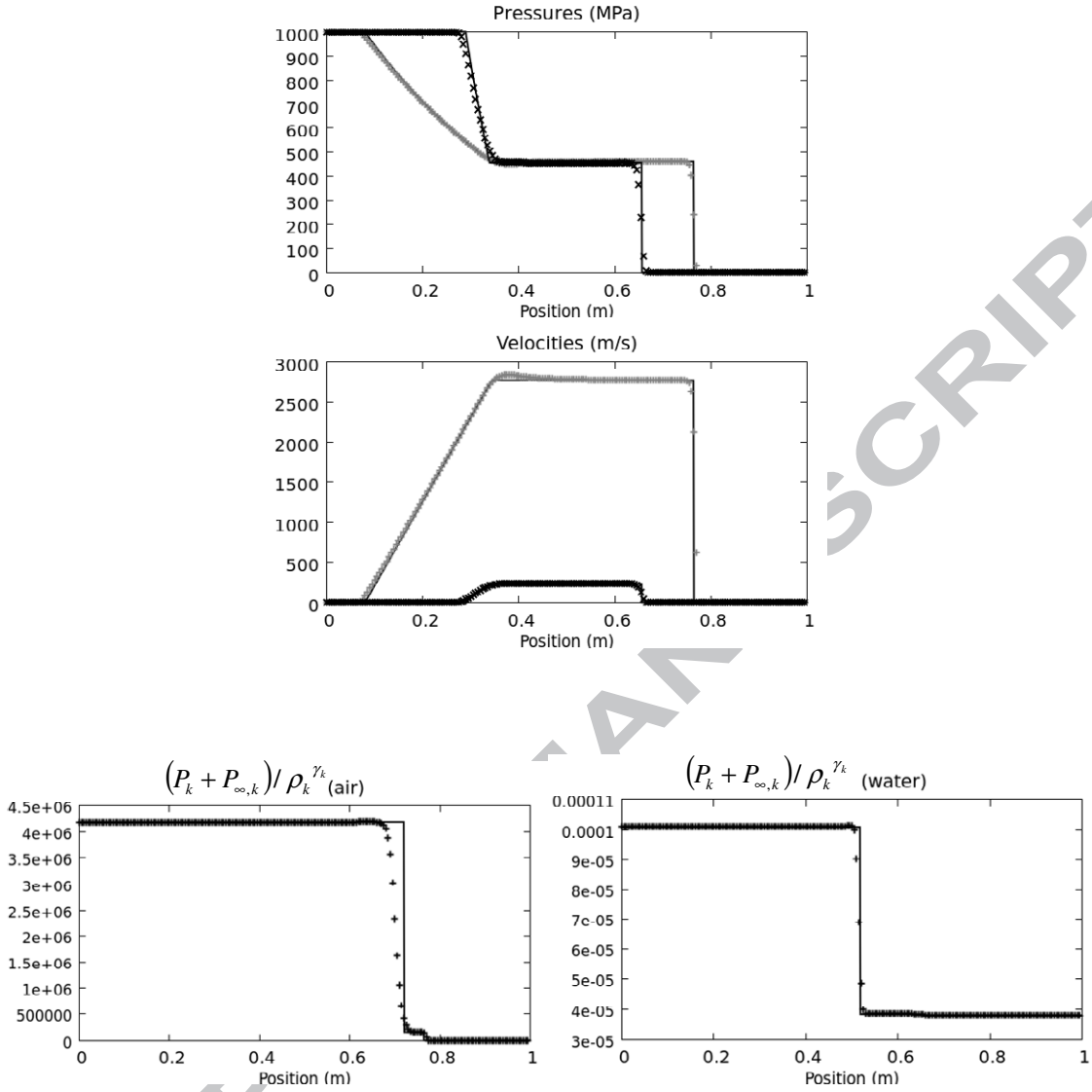

Figure 7: Two-phase shock tube with decoupled phase's evolutions. The initial volume fraction is uniform and relaxation effects are absent. The computations are made with the second order variant of the method, on a mesh involving 200 cells. Computed results are shown with symbols while exact ones are shown with lines.

The phase's entropy show correct agreement with the exact solution. As the volume fraction is uniform and relaxation effects absent, the wave u_I has no influence in the Riemann problem solution. The entropy of each phase varies across shocks and contact discontinuities and is nearly constant in rarefaction waves.

Two-phase shock tube with volume fraction discontinuity - Interface separating two fluids

In the left chamber, nearly pure liquid water ($\alpha_l = 1 - \varepsilon$ with $\varepsilon = 10^{-6}$) at the initial pressure of $2\times10^8 \mathrm{Pa}$ is settled while in the right chamber is filled with nearly pure air ($\alpha_l = \varepsilon$) at the initial pressure of $10^5 \mathrm{Pa}$. In both chambers, liquid and gas have the same densities $1000\ \mathrm{kg/m^3}$ and $50\ \mathrm{kg/m^3}$ respectively. A volume fraction discontinuity is located at x=0.8 m and separates the high and low pressure chambers.

Computed results obtained with the second order scheme are shown in Figure 8 at time $276\mu\mathrm{s}$. The numerical solution in symbols is compared to the exact solution.

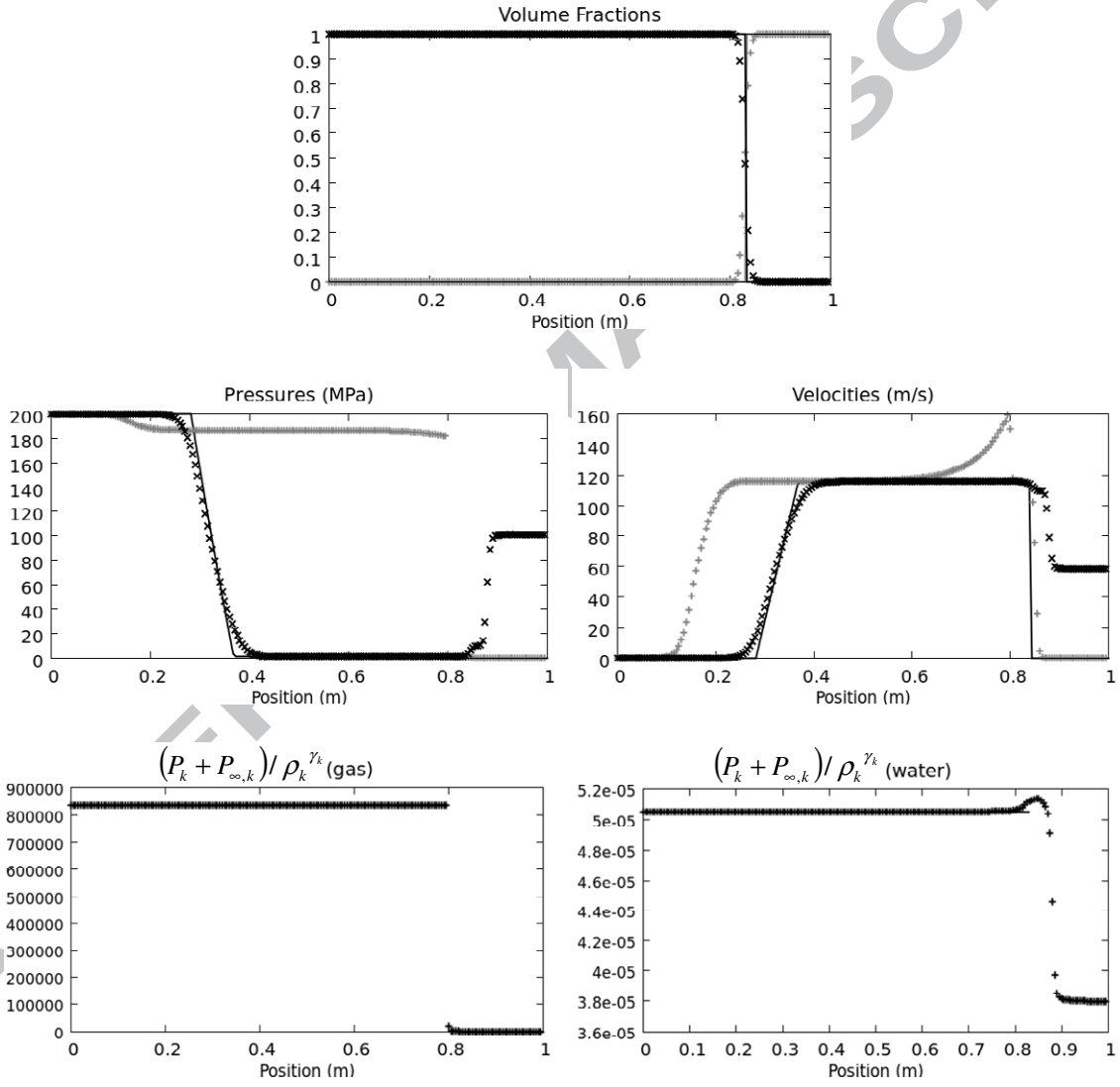

Figure 8: Shock tube with an interface separating nearly pure liquid water and nearly pure gas. Computed results (in symbols) are compared to exact solution (in lines). Relaxation effects are absent. The computations are made with the second order variant of the method, on a mesh involving 200 cells.

In absence of relaxation terms, each fluid evolves with its own pressure and velocity as there is no interaction between fluids. This test puts in evidence the contribution of the non-conservative terms. In the left part of the shock tube, the liquid is nearly pure and is expanded by a strong rarefaction wave. The solution of this rarefaction wave is in excellent agreement with the exact one obtained with a pure liquid on the left and a pure gas on the right. In the left part of the shock tube, the gas is expanded too. It accelerates near the interface because its volume varies in space and time (gray symbols). In the right part of the shock tube, a shock wave propagates in the gas due to the liquid–gas interface motion. The gas variables are in good agreement with the exact solution. The liquid present in the right chamber with a negligible volume is also accelerated by the right facing shock wave (dark symbols). It can be noted that the liquid entropy in the right chamber increases exaggeratedly. But it occurs in a zone where the liquid is in very small proportions. This exaggerated entropy increase improves method's robustness and has no consequences on its accuracy.

The most important point is that interfacial pressure and velocity are perfectly matched, as shown in Figure 9. These results show that the numerical method is able to deal with multiphase mixtures in non-equilibrium velocities as well as interface problems separating pure or nearly pure materials. Interface conditions are matched as a consequence of non-conservative terms and do not need relaxation ones, that are absent in the present computations.

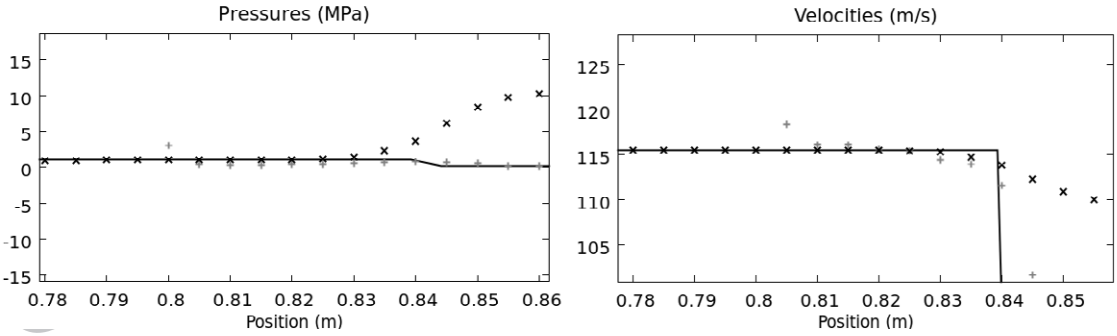

Figure 9: Magnified view of the pressure and velocity profiles obtained by the new method in the neighborhood of the interface. At position 0.8m perfect matching of the gas variables (gray symbols) and water ones (dark symbols) is clearly visible. Exact solutions are shown with lines.

Double expansion of a two-phase mixture

The initial volume fraction of the fluids is initially set to 0.5 everywhere, as well as densities and pressure of the fluids that are set uniform. The gas and liquid densities are respectively set to $10\,\mathrm{kg/m^3}$ and $1000\,\mathrm{kg/m^3}$. The pressure is set to 0.1 MPa. The initial velocities only are discontinuous at the domain centre. The two phases at left have the initial velocity of $-1000\,\mathrm{m/s}$ while the right part is set to $1000\,\mathrm{m/s}$. Results are shown at time $207\mu\mathrm{s}$ in Figure 10 and are obtained with the second order version of the method with Minmod limiter. The relative velocity is defined as the difference of the gas and liquid velocities. Stiff pressure relaxation is used everywhere contrarily to velocity drag that is absent. The results are shown in Figure 8 and compared to those of the DEM. This test is done with a uniform mesh involving 200 cells.

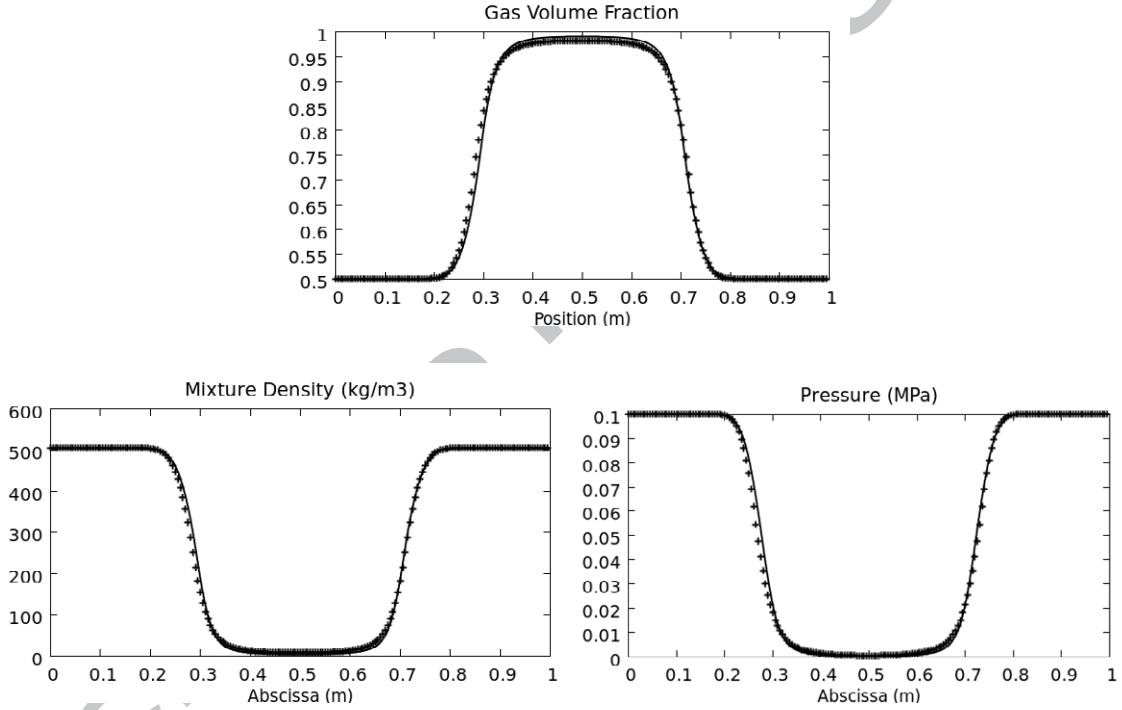

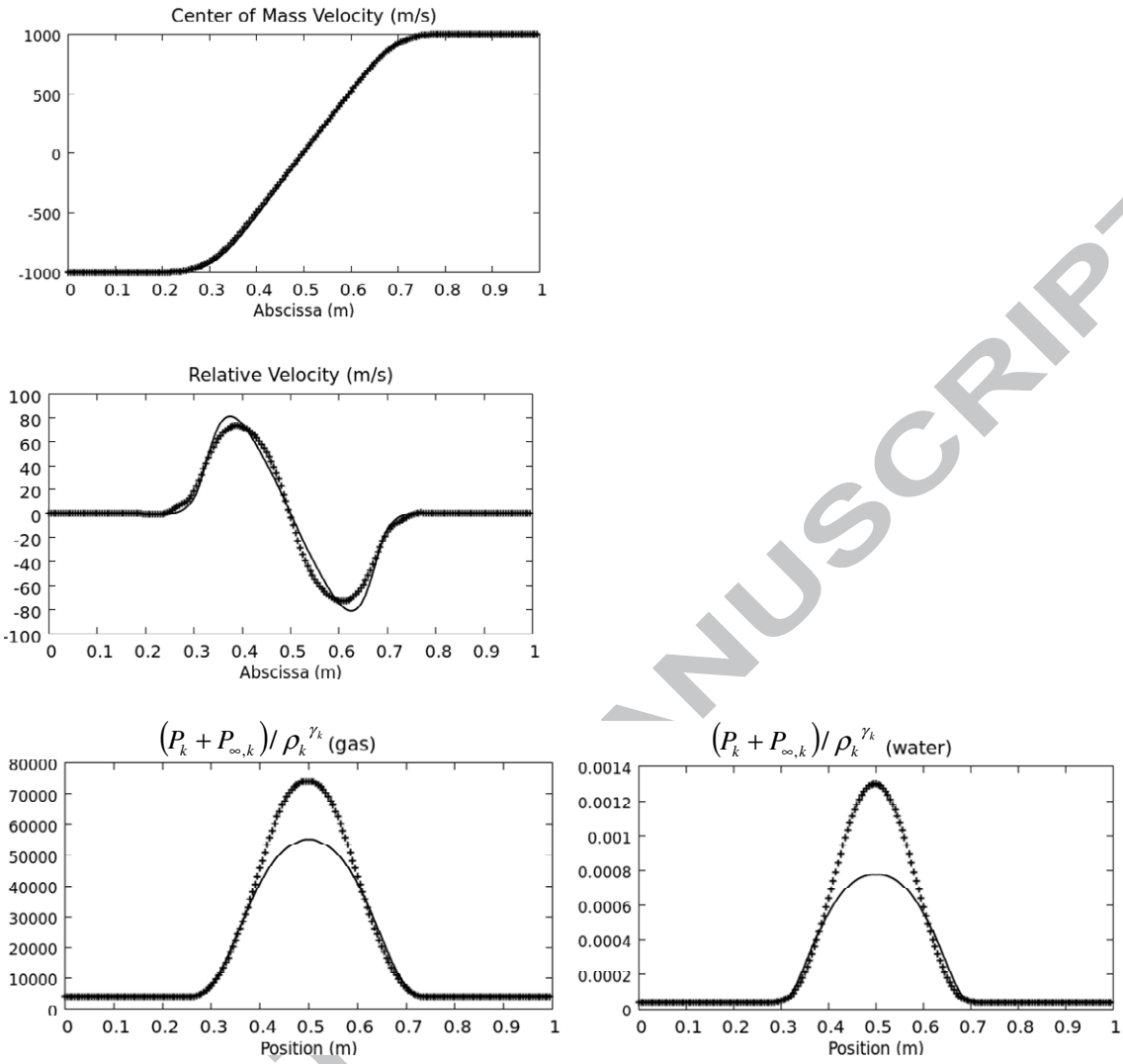

Figure 10: Double expansion test. Results of the new method are shown with symbols while those of the DEM are shown with lines. Large volume fraction increase appears at the tube center, as a consequence of pressure relaxation effects. Relative velocity also appears as a consequence of compressibility differences among the fluids. Results of the new method and those of the DEM are in good agreement. The new method produces more entropy than the DEM on this test problem. It is worth to mention that entropy is produced in this test mainly across the interfaces (volume fraction gradient zones) that appear dynamically.

Sedimentation test problem

A 1 m height vertical tube is considered, filled with liquid water and air. The tube is closed at both ends. The initial volume fraction is set to 0.5 for both fluids, the pressure is set uniform to $10^5 \mathrm{Pa}$ as well as fluid's densities that are set to $1\,\mathrm{kg/m^3}$ for the gas and $1000\,\mathrm{kg/m^3}$ for the liquid.

At $t=0$ the two-phase mixture is subjected to gravity $g=10\mathrm{m/s^{-2}}$ acceleration. The heavy fluid falls down and the light one goes up. At equilibrium, the lower half tube is filled with water and the upper one with air. The results are shown in Figure 11 and show that the method is able to separate phases.

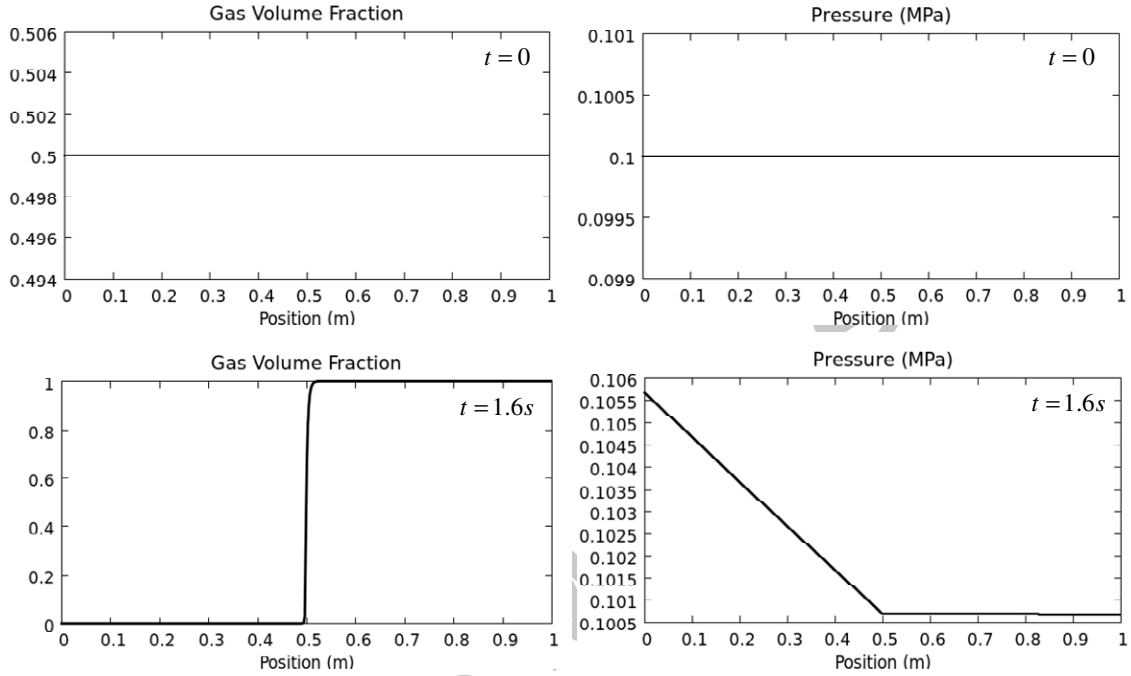

Figure 11: Sedimentation test problem. Initial data are shown in the upper graphs and the computed equilibrium state, reached after 1.6s is shown on bottom graphs.

Rogue et al. (1998) test problem

A vertical shock tube filled with air is considered as shown in Figure 12. A 2 cm particles bed is settled on a grid and is set to motion when the incident shock interacts with it. A wave refraction process occurs simultaneously: a transmitted shock propagates in the particles bed while a reflected shock wave is emitted. During particle motion, gas and particles have intense relative motion.

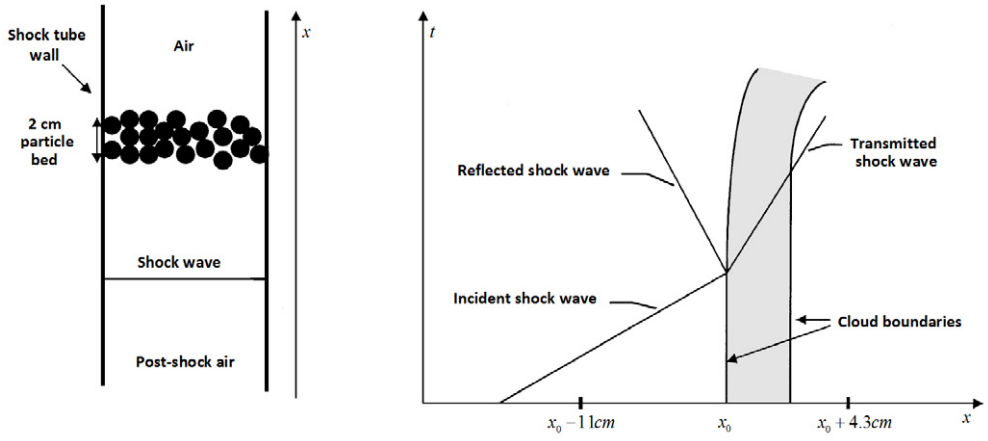

Figure 12 : Schematic representation of the experimental facility of Rogue et al. (1998). A vertical shock tube is filled with air and a particle bed is settled on a grid. The incident shock wave interacts with the particle bed and induces its motion while reflected and transmitted shock waves are emitted.

Two pressure gauges are used to record the pressure history at two locations, before ($x_0 - 11\,\mathrm{cm}$) and after ($x_0 + 4.3\,\mathrm{cm}$) the particles bed. These pressures signals are used to validate the present computations.

In the present computations, solid particles are considered compressible and governed by the SG EOS, with the same parameters as water, as their compressibility is weak in the present pressure range.

In the following notations lowerscripts a and p represent respectively the air and particles.

Particles drag effects are modelled by the force, $F = A_I f_d$, where $A_I = 6\alpha_p / d_p$ represents the specific interfacial area and d_p represents the particles diameter.

The unit drag force f_d is expressed by Ergun (1952) correlation when the granular bed in compacted $(\alpha_p \geq \alpha_{cr})$ and by Bernecker and Price (1974) correlation when it becomes dilute:

$$f_d = \frac{1}{6\alpha_a}\rho_a (u_a - u_p)|u_a - u_p| C_d ,$$

$$C_d = \begin{cases} \dfrac{150\alpha_p}{R_e} + 1.75 & \alpha_p \geq \alpha_{cr} \\ \dfrac{150\,\alpha_p}{R_e} + 1.75\left[\dfrac{(1-\alpha_{cr})\alpha_p}{\alpha_{cr}\alpha_a}\right]^{0.45} & (1-\alpha_S) \leq \alpha_p < \alpha_{cr} \\ \dfrac{150\alpha_p}{R_e} + 0.3 & \alpha_p < (1-\alpha_S) \end{cases}$$

with $\alpha_S = \left(1+0{,}02\times\frac{1-\alpha_{cr}}{\alpha_{cr}}\right)^{-1}$ and $\alpha_{cr} = 0.63$.

In these formulas the particles Reynolds number is defined as: $R_e = \frac{d_p \alpha_a \rho_a |u_a - u_p|}{\mu_a}$.

Table 1 summarizes experimental data.

Parameter	**Value**
Air preshock density	$1.2\ \mathrm{kg/m^3}$
Incident shock Mach number	1.3
Particle density	$1050\ \mathrm{kg/m^3}$
Particle diameter (d_p)	$2\ \mathrm{mm}$
Particle bed thickness	$2\ \mathrm{cm}$
Initial gas volume fraction in the bed	0.35
Air viscosity (μ_a)	$2\times10^{-5}\ \mathrm{Pa.s}$

Table 1. Data of the Rogue et al. (1998) two-phase shock tube test.

The Rogue et al. (1998) pressure signals (grey symbols) are compared to the present computations (black symbols) in Figure 13, showing correct agreement. The computations are done with a mesh involving 1500 cells. Stiff pressure relaxation is used.

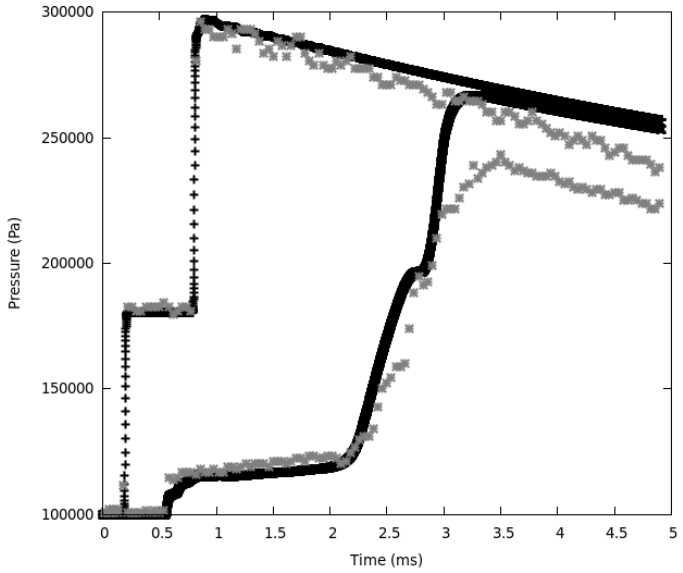

Figure 13: Comparison of recorded and computed pressure signals at the two pressure gauges for the Rogue test problem.

7.2 Velocity equilibrium two-phase flow tests

All tests that follow are done with a uniform mesh involving 200 cells. In these computations, both stiff pressure and velocity relaxation solvers of the Appendix C and D are used. Moreover, computed results are obtained with the second order method of Appendix B and Minmod limiter.

Interface separating two fluids

In the left chamber, nearly pure liquid water ($\alpha_l = 1 - \varepsilon$ with $\varepsilon = 10^{-6}$) at the initial pressure of $2\times10^8 \text{Pa}$ is settled while the right chamber is filled with nearly pure air ($\alpha_l = \varepsilon$) at the initial pressure of 10^5Pa. In both chambers, liquid and gas have the same densities $1000\,\text{kg/m}^3$ and $50\,\text{kg/m}^3$ respectively. A volume fraction discontinuity thus separates the high and low pressure chambers.

Computed results are shown in Figure 14 at time $291\,\mu\text{s}$. The numerical solution in symbols is compared to the exact one, determined from the Euler equations as both media are nearly pure.

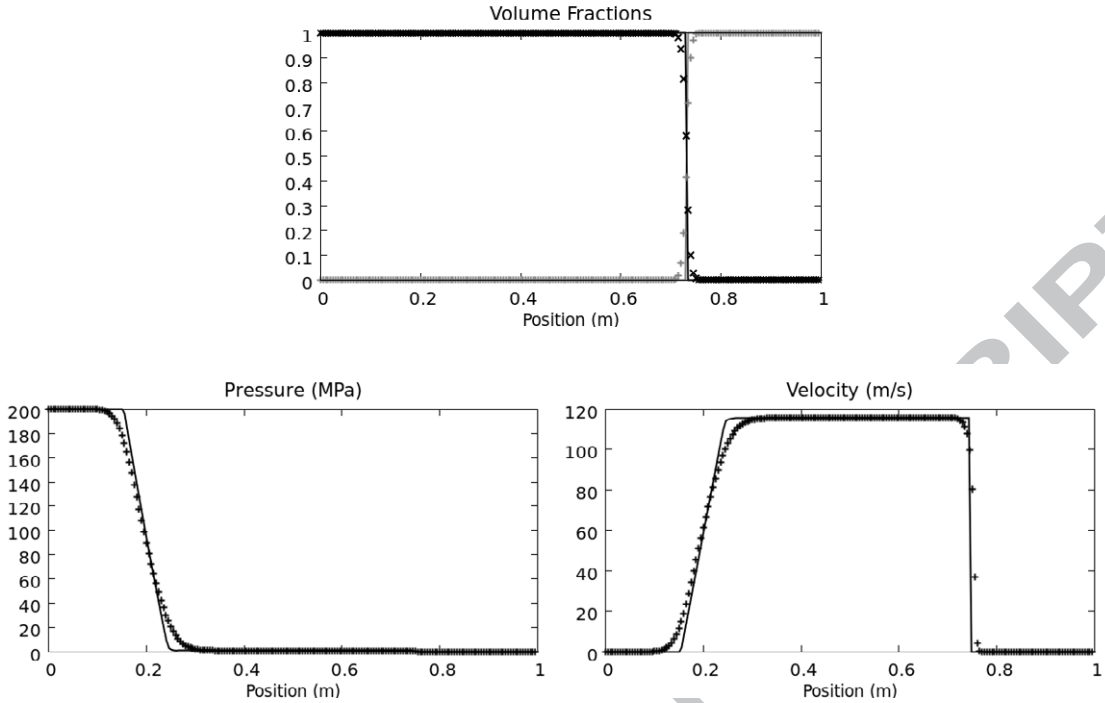

Figure 14: Shock tube with an interface separating nearly pure liquid water and nearly pure gas. Computed results (in symbols) are compared to the exact solution of the Euler equations (in lines). Perfect matching of interface conditions is observed, thanks to the stiff velocity and pressure relaxation solvers.

Shock tube with two mixtures

We now consider a mixture of two condensed phases, liquid water and aluminium. EOS parameters for the aluminium phase are $\gamma_{Al} = 3.4$ and $P_{\infty,Al} = 21.5\times10^{9}\,\mathrm{Pa}$ while for the liquid EOS parameters are unchanged. The volume fraction is set initially uniform ($\alpha_{Al} = 0.5$). The left chamber has the same high pressure for both phases ($10^{9}\,\mathrm{Pa}$) while the right one has the same low pressure ($10^{5}\,\mathrm{Pa}$) for both phases. Aluminium and liquid densities are respectively set to $2700\,\mathrm{kg/m^3}$ and $1000\,\mathrm{kg/m^3}$.

Stiff pressure and velocity relaxation is considered everywhere. In this context, volume fractions vary in both compression and expansion waves.

The limit model that is solved with the present method corresponds to the mechanical equilibrium model of Kapila et al. (2001). Computed results are shown with symbols in Figure 15 at time $111\,\mu\mathrm{s}$. They are compared to the exact solution of the Kapila model given in Petitpas et al. (2007).

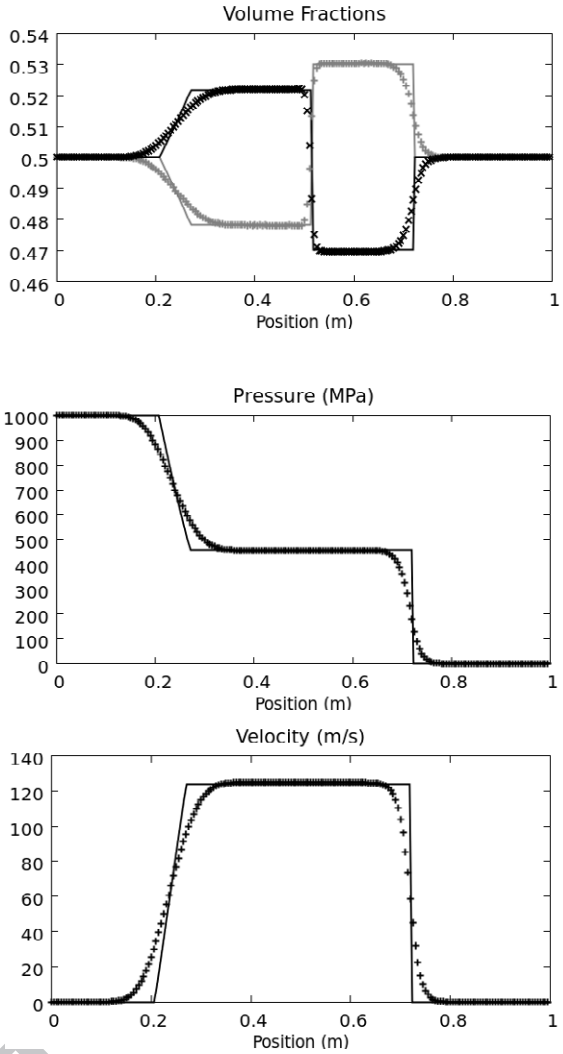

Figure 15: Shock tube with a high pressure chamber on the left containing a two-phase mixture and a low pressure chamber on the right filled by the same two-phase mixture. The computed results with the HLLC solver + mechanical relaxation in symbols are compared to the exact solution in lines, showing excellent agreement.

7.3. 3D Computations

3D extension of the method follows the lines of Toro (2009) pp 578-584. In this bookchapter, finite volume methods for hyperbolic systems of conservation laws are summarized. Here, the method is developped in the 3D code ($d\alpha dt^{TM}$) based on unstructured meshes made of tetrahedrons. The present HLLC solver is used to compute the cell boundary fluxes along the face normal vector.

Explosive liquid water experiments

The experimental facility is schematized in Figure 16. It consists in a solid explosive cylinder surrounded by liquid water. As the explosive detonation is very fast, constant volume explosion assumption is used to compute gas detonation products pressure, that is about 70 Kbars. From this kind of cylindrical shock tube, a complex 3D flow emerges with gas jets along the symetry axis and particles radial jets, as shown in Figure 17.

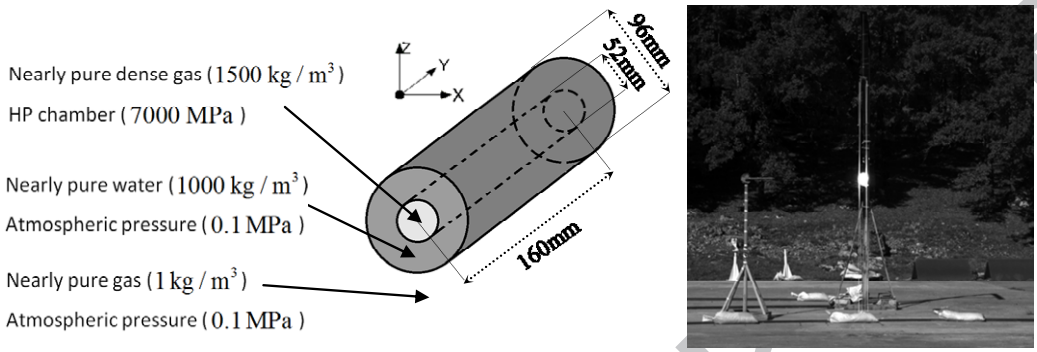

Figure 16 : Schematic representation of the cylindrical gas-liquid explosion facility made at CEA Gramat. A cylindrical explosive charge is surrounded by a liquid water layer. The system is suspended in air as shown in the right photograph, fired and recorded with ultra fast cameras.

To achieve 3D computations of this test problem the $\mathrm{d}\alpha\mathrm{dt}^{\mathrm{TM}}$ code is used with a mesh made of 2.383.176 tetrahedrons and with $\mathrm{CFL} = 0.5$.

In the following, front and side views of liquid water clouds are shown at two times in Figures 17 and 18. Numerical results are qualitatively compared to the experimental photographs, showing both good agreement and capabilites of the method.

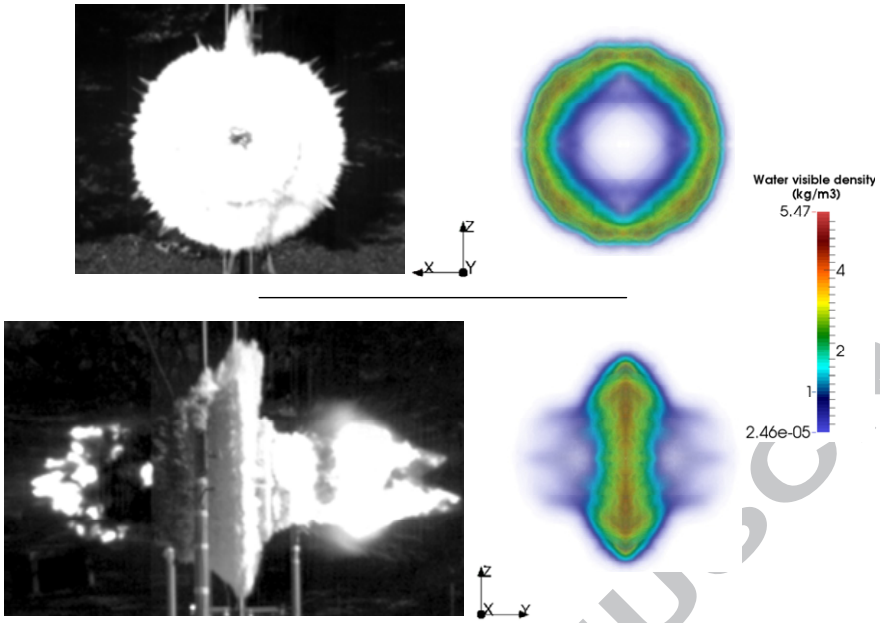

Figure 17 : Comparison between experimental photographs (left) and numerical results (right) showing liquid droplet clouds at time $480\mu s$

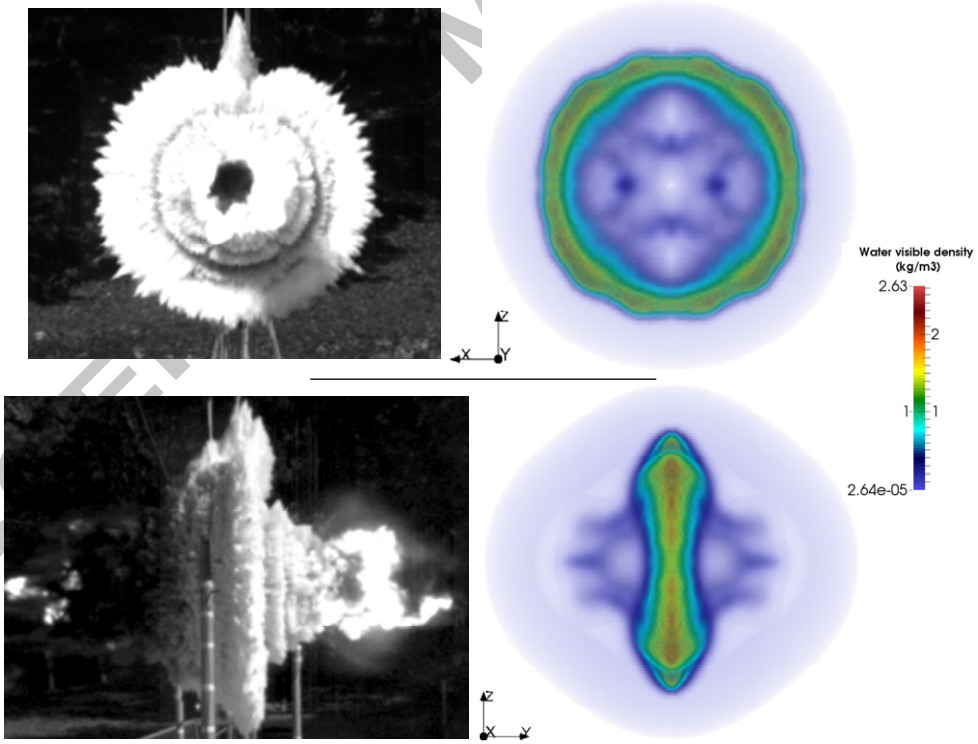

Figure 18 : Same comparison as in the former figure showing liquid droplet clouds at time $1000\mu s$

The method is thus able to deal with three-dimensional complex two-phase flows in the presence of high pressure , density and velocity gradients.

8. Conclusion

A new method has been built to solve non-equilibrium two-phase flows. This method is simpler than existing Godunov type schemes in this area and is of comparable accuracy and robustness as the DEM.

When dealing with a larger number of fluids, the new method is expected to be more and more efficient as it uses a single HLLC resolution per phase, while the DEM uses N^2 Riemann problem resolutions, where N represents the number of fluids. Also, its extension to implicit schemes seems much more tracktable than with the DEM.

Acknowledgements

The authors would like to thank the anonymous referees for their many constructive comments and suggestions that definitely helped to improve the quality of this article. They also thank the Editors for their management of the review.

This work has been carried out in the framework of the Labex MEC (ANR-10-LABX-0092) and of the A*MIDEX project (ANR-11-IDEX-0001-02), funded by the « Investissements d'Avenir » French Government program managed by the French National Research Agency (ANR).

References

R. Abgrall and R. Saurel, Discrete equations for physical and numerical compressible multiphase mixtures, J. Comput. Phys. 186 (2003) 361–396.

A. Ambroso, C. Chalons and P.-A. Raviart, A Godunov-type method for the seven-equation model of compressible two-phase flow, Computers and Fluids 54 (2012) 67–91

N. Andrianov and G. Warnecke, The Riemann problem for the Baer–Nunziato model of two-phase flows, J. Comput. Phys. 195 (2004) 434–464

M. R. Baer and J.W. Nunziato, A two-phase mixture theory for the deflagration-to-detonation transition (DDT) in reactive granular materials, J. Multiphase Flow 12 (1986) 861–889

R. R. Bernecker and D. Price, Studies in the transition from deflagration to detonation in granular explosives – III – Proposed mechanisms for transition and comparison with other proposals in the literature, Combust. Flame, 22 (1974) p. 161

R. A. Berry, R. Saurel and O. Le Metayer, The discrete equation method (DEM) for fully compressible, two-phase flows in ducts of spatially varying cross-section, Nuclear Engineering and Design 240 (2010) 3797-3818

F. Bouchut, Nonlinear stability of finite volume methods for hyperbolic conservation laws, and well-balanced schemes for sources, Frontiers in Mathematics series, Birkhäuser, 2004

C-H. Chang and M-S. Liou, A robust and accurate approach to computing compressible multiphase flow: Stratified flow model and AUSM+-up scheme, J. Comput. Phys. 225 (2007) 840-873

A. Chinnayya, E. Daniel and R. Saurel, Computation of detonation waves in heterogeneous energetic materials, Journal of Computational Physics 196 (2004) 490–538.

S. F. Davis, Simplified second-order Godunov-type methods. SIAM J. Sci. and Stat. Comput. 9:445 (1988)

V. Deledicque and M.V. Papalexandris, An exact Riemann solver for compressible two-phase flow models containing non-conservative products, J. Comput. Phys. 222 (2007) 217–245

M. Dumbser, A. Hidalgo, M. Castro, C. Parés and E.F. Toro. FORCE Schemes on Unstructured Meshes II: Non-Conservative Hyperbolic Systems. Computer Methods in Applied Mechanics and Engineering, 199 (9-12):625-647, 2010.

M. Dumbser and E.F. Toro. A Simple Extension of the Osher Riemann Solver to Non-Conservative Hyperbolic Systems. Journal of Scientific Computing, 48:70-88, 2011

S. Ergun, Fluid flow through packed columns, Chem Eng Progress 48 (1952)

SK. Godunov, A finite difference method for numerical calculation of discontinuous solutions of the equation of fluid dynamics, Matematicheskii Sbornik 47 (1959) 271–306

A. Harten, P. Lax and B. van Leer, On upstream differencing and Godunov-type schemes for hyperbolic conservation laws. SIAM (1983), Rev. 25, 35-61

A. K. Kapila, R. Menikoff, J.B. Bdzil, S.F. Son and D.S. Stewart, Two-phase modeling of deflagration-to-detonation transition in granular materials: reduced equations, Physics of Fluids 13 (10) (2001) 3002–3024

M-H. Lallemand and R. Saurel, Pressure relaxation procedures for multiphase compressible flows, INRIA Report 4038 (2000)

O. Le Metayer, J. Massoni and R. Saurel, Modeling evaporation fronts with reactive Riemann solvers, Journal of Computational Physics 205 (2005) 567–610.

Q. Li, H. Feng, T. Cai and C. Hu, Difference scheme for two-phase flow, Applied Mathematics and Mechanics 25 (2004) 536–545

S. Liang, W. Liu and L. Yuan, Solving seven-equation model for compressible two-phase flow using multiple GPUs, Computers & Fluids (2014)

S. Osher and F. Solomon, Upwind difference schemes for hyperbolic conservation laws. Math. Comput. 38, 339–374 (1982)

C. Parés, Numerical methods for nonconservative hyperbolic systems: a theoretical framework, SIAM J. Numer. Anal. 44 (2006) 300–321

F. Petitpas, E. Franquet, R. Saurel and O. Le Metayer, A relaxation-projection method for compressible flows. Part II: Artificial heat exchanges for multiphase shocks. Journal of Computational Physics, 225(2) (2007) 2214-2248

X. Rogue, G. Rodriguez, J.F. Haas and R. Saurel, Experimental and numerical investigation of the shock-induced fluidization of a particle bed, Shock Waves, 8 (1998), pp. 29–45

R. Saurel and R. Abgrall, A multiphase Godunov method for compressible multifluid and multiphase flows, J. Comput. Phys. 150 (1999) 425–467

R. Saurel, S. Gavrilyuk and F. Renaud, A multiphase model with internal degrees of freedom: application to shock–bubble interaction. Journal of Fluid Mechanics (2003), 495, pp 283-321

R. Saurel, O. Le Metayer, J. Massoni and S. Gavrilyuk, Shock jump relations for multiphase mixtures with stiff mechanical relaxation, Shock Waves 16 (3) (2007) 209–232

R. Saurel, F. Petitpas and R. A. Berry, Simple and efficient relaxation methods for interfaces separating compressible fluids, cavitating flows and shocks in multiphase mixtures, J. Comput. Phys. 228 (2009) 1678-1712

D.W. Schwendeman, C.W. Wahle and A.K. Kapila, The Riemann problem and a high-resolution Godunov method for a model of compressible two-phase flow, J. Comput. Phys. 212 (2006) 490–526

S. Tokareva and E. F. Toro, HLLC-type Riemann solver for the Baer-Nunziato equations of compressible two-phase flow, J. Comput. Phys. 229 (2010) 3573–3604

E. F. Toro, A weighted average flux method for hyperbolic conservation laws. Proceedings of the Royal Society of London. A. Mathematical and Physical Sciences, vol. 423, num 1865 (1989) 401-418.

E.F. Toro, M. Spruce and W. Speares, Restoration of the contact surface in the HLL-Riemann solver, Shock Waves 4 (1994) 25–34

E. F. Toro, Riemann Solvers and Numerical Methods for Fluid Dynamics, Springer-Verlag, 1997

E.F. Toro, S.J. Billet, Centered TVD schemes for hyperbolic conservation laws, IMA J. Numer. Anal. 20 (2000) 44–79

B. Van Leer, Toward the ultimate conservation difference scheme V, A second order sequel to Godunov's method. J Comput Phys 32 (1979) 101–136

A. Zein, M. Hantke and G. Warnecke, Modeling phase transition for compressible two-phase flows applied to metastable liquids, J. Comput. Phys. 229 (2010) 2964–2998

Appendix A. HLLC Riemann solver when $S_{L,k} < u_I < S_{M,k} < S_{R,k}$

The corresponding wave pattern is recalled in Figure A.1.

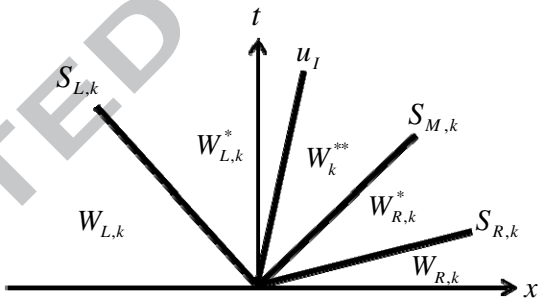

Figure A.1: Wave pattern configuration when $S_{L,k} < u_I < S_{M,k} < S_{R,k}$ in the frame of HLLC approximation.

The Rankine-Hugoniot relations applied to the locally conservative system (5) read:

$$F^*_{L,k} = F_{L,k} + S_{L,k}\left(U^*_{L,k} - U_{L,k}\right),$$

$$F^*_{R,k} = F_{R,k} + S_{R,k}\left(U^*_{R,k} - U_{R,k}\right),$$

$$F^{**}_k = F^*_{R,k} + S_{M,k}\left(U^{**}_k - U^*_{R,k}\right),$$

$$F^{*}_{L,k} = F^{**}_{k} + u_I\left(U^{*}_{L,k} - U^{**}_{k}\right).$$

Vectors $U^{*}_{L,k}$, $U^{*}_{R,k}$ and U^{**}_{k} are determined following the same strategy as in Section 4.2.

- **State** $W^{*}_{R,k}$

$$\alpha^{*}_{R,k} = \alpha_{R,k},$$

$$(\alpha\rho)^{*}_{R,k} = (\alpha\rho)_{R,k}\frac{u_{R,k} - S_{R,k}}{S_{M,k} - S_{R,k}},$$

$$u^{*}_{R,k} = S_{M,k},$$

$$P^{*}_{R,k} = P_{R,k} + \rho_{R,k}\left(u_{R,k} - S_{R,k}\right)\left(u_{R,k} - S_{M,k}\right),$$

$$E^{*}_{R,k} = E_{R,k} + \frac{(Pu)_{R,k} - P^{*}_{R,k}S_{M,k}}{\rho_{R,k}\left(u_{R,k} - S_{R,k}\right)}.$$

- **State** $W^{*}_{L,k}$

$$\alpha^{*}_{L,k} = \alpha_{L,k},$$

$$(\alpha\rho)^{*}_{L,k} = (\alpha\rho)_{L,k}\frac{u_{L,k} - S_{L,k}}{S_{M,k} - S_{L,k}},$$

$$u^{*}_{L,k} = S_{M,k},$$

$$P^{*}_{L,k} = P_{L,k} + \rho_{L,k}\left(u_{L,k} - S_{L,k}\right)\left(u_{L,k} - S_{M,k}\right),$$

$$E^{*}_{L,k} = E_{L,k} + \frac{(Pu)_{L,k} - P^{*}_{L,k}S_{M,k}}{\rho_{L,k}\left(u_{L,k} - S_{L,k}\right)}.$$

- **State** W^{**}_{k}

$$\alpha^{**}_{k} = \alpha_{R,k},$$

$$(\alpha\rho)^{**}_{k} = (\alpha\rho)^{*}_{L,k},$$

$$u^{**}_{k} = S_{M,k},$$

$$P_k^{**} = P_{R,k}^{*} \quad \text{ou} \quad P_k^{**} = \frac{\alpha_{L,k}}{\alpha_{R,k}} P_{L,k}^{*} + \frac{\alpha_{R,k} - \alpha_{L,k}}{\alpha_{R,k}} P_I \quad ,$$

$$E_k^{**} = E_{L,k}^{*} - \frac{\alpha_{R,k} - \alpha_{L,k}}{(\alpha\rho)_{L,k}^{*}} P_I \, .$$

Appendix B. Second-order extension

The first order Godunov method of Section 6 is extended to higher order with the MUSCL-Hancock strategy.

System (4) is recalled hereafter :

$$\frac{\partial U_k}{\partial t} + \frac{\partial F_k}{\partial x} + \alpha_k \frac{\partial H_k}{\partial x} = 0 \, , \ \forall k \in \{1,2\},$$

with $U_k = \begin{pmatrix} \alpha_k \\ (\alpha\rho)_k \\ (\alpha\rho u)_k \\ (\alpha\rho E)_k \end{pmatrix}$, $F_k = \begin{pmatrix} \alpha_k u_I \\ (\alpha\rho u)_k \\ \alpha_k (\rho u^2 + P)_k - \alpha_k P_I \\ \alpha_k (\rho E + P)_k u_k - \alpha_k P_I u_I \end{pmatrix}$ and $H_k = \begin{pmatrix} -u_I \\ 0 \\ P_I \\ P_I u_I \end{pmatrix}$.

The set of primitive variables, Ψ_k reads $\Psi_k = (\alpha_k, \ \rho_k, \ u_k, \ P_k)^T$.

The MUSCL method proceeds with the following sequence.

Riemann problem resolution for the locally conservative System (5)

The Riemann problem is solved with the extrapolated variables and the cell boundary flux is computed as $F_{k,i\pm\frac{1}{2}}^{*} = F_{k,i\pm\frac{1}{2}}^{*}\left(\Psi_L^n, \Psi_R^n\right)$. Moreover, the computation of u_I^n and P_I^n provides the non-conservative flux $H_{k,i\pm\frac{1}{2}}^{*}$.

Gradients computation

Let us denote by $\Delta_{k,i}^{-}$ and $\Delta_{k,i}^{+}$ the gradients computed on the left and right sides of computational cell i:

$$\Delta_{k,i}^{-} = \frac{\Psi_{k,i}^n - \Psi_{k,i-1}^n}{\Delta x} \text{ and } \Delta_{k,i}^{+} = \frac{\Psi_{k,i+1}^n - \Psi_{k,i}^n}{\Delta x} \, .$$

A slope limiter ξ is used to avoid local extrema. In the present work, MinMod and Van Leer limiters are used.

After limitation, the slope is denoted by $\Delta_{k,i} = \xi\left(\Delta_{k,i}^{-}, \Delta_{k,i}^{+}\right)$.

Godunov type scheme during half time step

$$U_{k,i}^{n+1/2} = U_{k,i}^{n} - \frac{\Delta t^{n}}{2\Delta x}\left[F_{k,i+\frac{1}{2}}^{*} - F_{k,i-\frac{1}{2}}^{*} + \alpha_{k,i}^{n}\left(H_{k,i+\frac{1}{2}}^{*} - H_{k,i-\frac{1}{2}}^{*}\right)\right],\ \forall k \in \{1,2\}$$

Variables extrapolation

For a given cell boundary $i+1/2$ at time $t^{n+1/2}$, left and right extrapolated states are given by :

$$\Psi_{L,k}^{n+1/2} = \Psi_{k,i}^{n+1/2} + \frac{\Delta x}{2}\Delta_{k,i} \text{ and } \Psi_{R,k}^{n+1/2} = \Psi_{k,i+1}^{n+1/2} - \frac{\Delta x}{2}\Delta_{k,i+1}.$$

Riemann problem resolution for the locally conservative System (5)

The Riemann problem is solved with the extrapolated variables and the cell boundary flux is computed as $F_{k,i\pm\frac{1}{2}}^{**} = F_{k,i\pm\frac{1}{2}}^{*}\left(\Psi_{L}^{n+1/2}, \Psi_{R}^{n+1/2}\right)$. Moreover, the computation of $u_{I}^{n+1/2}$ and $P_{I}^{n+1/2}$ provide the non-conservative flux $H_{k,i\pm\frac{1}{2}}^{**}$.

Evolution step

$$U_{k,i}^{n+1} = U_{k,i}^{n} - \frac{\Delta t}{\Delta x}\left[F_{k,i+\frac{1}{2}}^{**} - F_{k,i-\frac{1}{2}}^{**} + \alpha_{k,i}^{n+1/2}\left(H_{k,i+\frac{1}{2}}^{**} - H_{k,i-\frac{1}{2}}^{**}\right)\right],\ \forall k \in \{1,2\}.$$

Appendix C. Stiff velocity relaxation solver

Stiff velocity relaxation is considered after wave dynamics, considered in the hyperbolic solver. When stiff drag interaction only is present, the system to solve is:

Phase1	Phase2	
$\frac{\partial \alpha_1}{\partial t} = 0$	$\frac{\partial \alpha_2}{\partial t} = 0$	
$\frac{\partial \alpha_1\rho_1}{\partial t} = 0$	$\frac{\partial \alpha_2\rho_2}{\partial t} = 0$	(C.1)
$\frac{\partial \alpha_1\rho_1 u_1}{\partial t} = \lambda(u_2 - u_1)$	$\frac{\partial \alpha_2\rho_2 u_2}{\partial t} = -\lambda(u_2 - u_1)$	
$\frac{\partial \alpha_1\rho_1 E_1}{\partial t} = \lambda\overline{u_I}(u_2 - u_1)$	$\frac{\partial \alpha_2\rho_2 E_2}{\partial t} = -\lambda\overline{u_I}(u_2 - u_1)$	

Knowledge of the drag coefficient λ is useless in the stiff velocity relaxation limit as this parameter is going to disappear. In this limit, $\lambda \to +\infty$.

The system above implies mass conservation for each phase and for the mixture:

$$(\alpha\rho)_k = \text{cte}$$

$$\rho = \sum_{k=1}^{2} (\alpha\rho)_k = \text{cte}$$

Consequently, mass fractions are constants during the relaxation process: $Y_k = \frac{(\alpha\rho)_k}{\rho} = \text{cte}$.

The velocity at relaxation is readily obtained as,

$$u^* = \sum_{k=1}^{2} Y_k^0 u_k^0 ,$$

where the superscript 0 denotes the state before relaxation (at the end of the hyperbolic step).

Combining the total energy and momentum equations of System (C.1) the following identities are obtained,

$$\frac{\partial(\alpha\rho E)_k}{\partial t} = \overline{u_I} \frac{\partial(\alpha\rho u)_k}{\partial t} .$$

With the help of mass conservation equations of the phases they become,

$$\frac{\partial E_k}{\partial t} = \overline{u_I} \frac{\partial u_k}{\partial t} .$$

As the relaxed velocity $u^* = \sum_{k=1}^{2} Y_k^0 u_k^0$ is a constant during the relaxation process, we assume $\overline{u_I} = \text{cte} = u^*$.

Thanks to this assumption, the relaxed total energies read,

$$E_k^* = E_k^0 + u^* \left(u^* - u_k^0\right).$$

The associated relaxed internal energies read,

$$e_k^* = e_k^0 + \frac{1}{2}\left(u^* - u_k^0\right)\left(u^* - u_k^0\right).$$

Appendix D. Stiff pressure relaxation solver

After wave propagation, velocity relaxation or any evolution process the pressures are in disequilibrium. The pressure relaxation time is usually very short, less than one microsecond. Also, when dealing with interfacial flows, stiff pressure and velocity relaxation are needed to fulfil interface conditions.

The system to consider reads:

Phase 1

$$\frac{\partial \alpha_1}{\partial t} = \mu\left(P_1 - P_2\right)$$

$$\frac{\partial \alpha_1 \rho_1}{\partial t} = 0$$

$$\frac{\partial \alpha_1 \rho_1 u_1}{\partial t} = 0$$

$$\frac{\partial \alpha_1 \rho_1 E_1}{\partial t} = -\mu \overline{P_I}\left(P_1 - P_2\right)$$

Phase 2

$$\frac{\partial \alpha_2}{\partial t} = -\mu\left(P_1 - P_2\right)$$

$$\frac{\partial \alpha_2 \rho_2}{\partial t} = 0$$

$$\frac{\partial \alpha_2 \rho_2 u_2}{\partial t} = 0$$

$$\frac{\partial \alpha_2 \rho_2 E_2}{\partial t} = \mu \overline{P_I}\left(P_1 - P_2\right)$$

(D.1)

The pressure relaxation coefficient μ has been determined for example in Saurel et al. (2003). Here, it is assumed to tend to infinity, $\mu \to +\infty$.

System (D.1) implies mass invariance for each phase and for the mixture:

$$\left(\alpha\rho\right)_k = \text{cte}$$

$$\rho = \sum_{k=1}^{2} \left(\alpha\rho\right)_k = \text{cte}$$

Velocity of the phases stays invariant too.

Combining the total energy and volume fraction equations, the relaxation term vanishes,

$$\frac{\partial \left(\alpha\rho E\right)_k}{\partial t} = -\overline{P_I} \frac{\partial \alpha_k}{\partial t}.$$

With the help of the mass conservation equation of the phase it reduces to,

$$\frac{\partial E_k}{\partial t} = -\overline{P_I} \frac{\partial v_k}{\partial t},$$

where v_k denotes the specific volume of phase k.

Assuming $\overline{P_I} = P^*$, the relaxed pressure, integration of the former equations read,

$$E_k^* = E_k^0 - P^*\left(v_k^* - v_k^0\right),$$

or alternatively,

$$e_k^* = e_k^0 - P^*\left(v_k^* - v_k^0\right).$$

(D.2)

When each phase is governed by the 'stiffened-gas' equation of state (EOS) given by (27), the relaxed pressure is determined analytically. For other convex equation of state, an iterative method is needed (see for example Lallemand and Saurel, 2000).

Inserting the EOS in (D.2) a relation linking the pressure and the specific volume of the phases is obtained:

$$v_k^* = \frac{v_k^0}{\gamma_k}\left(\gamma_k - 1 + \frac{P_k^0 + P_{\infty,k}}{P^* + P_{\infty,k}}\right)$$

With the help of the mass invariance of the phases it becomes:

$$\alpha_k^* = \frac{\alpha_k^0}{\gamma_k}\left(\gamma_k - 1 + \frac{P_k^0 + P_{\infty,k}}{P^* + P_{\infty,k}}\right) = \alpha_k^0 + \frac{\alpha_k^0}{\gamma_k}\left(\frac{P_k^0 + P_{\infty,k}}{P^* + P_{\infty,k}} - 1\right)$$

The saturation constraint ($\sum_{k=1}^{2}\alpha_k^* = \sum_{k=1}^{2}\alpha_k^0 = 1$) provides the closure relation: $\sum_{k=1}^{2}\frac{\alpha_k^0}{\gamma_k}\left(\frac{P_k^0 + P_{\infty,k}}{P^* + P_{\infty,k}}\right) = \sum_{k=1}^{2}\frac{\alpha_k^0}{\gamma_k}$.

This equation admits a positive root: $P^* = \frac{1}{2}(A_1 + A_2 - P_{\infty,1} - P_{\infty,2}) + \sqrt{\frac{1}{4}(A_2 - A_1 - P_{\infty,2} + P_{\infty,1})^2 + A_1 A_2}$.

With the following notations, $A_1 = \dfrac{\frac{\alpha_1^0}{\gamma_1}(P_1^0 + P_{\infty,1})}{\frac{\alpha_1^0}{\gamma_1} + \frac{\alpha_2^0}{\gamma_2}}$ and $A_2 = \dfrac{\frac{\alpha_2^0}{\gamma_2}(P_2^0 + P_{\infty,2})}{\frac{\alpha_1^0}{\gamma_1} + \frac{\alpha_2^0}{\gamma_2}}$.

Appendix E. Non conservative terms in the numerical scheme – Other flow configurations

In Section 6, we showed agreement between the discrete form of the term $\alpha_k \frac{\partial H_k}{\partial x}$ and the DEM one. Demonstration was made in the case of a positive flow velocity at both cell boundaries and decreasing volume fraction profile. Let's now consider the other flow configurations, in order to justify in a general way the discrete form we use.

The calculations are specified for phase 1. We have to compare both expressions,

$$(\alpha H)^*_{l,i+\frac{1}{2}} - (\alpha H)^*_{l,i-\frac{1}{2}} - \alpha^n_{l,i}\left(H^*_{l,i+\frac{1}{2}} - H^*_{l,i-\frac{1}{2}}\right) =$$
$$= \left(\alpha^n_{l,i}\left(\frac{u_l^+}{|u_l|}\right)_{i+1/2} - \alpha^n_{l,i+1}\left(\frac{u_l^-}{|u_l|}\right)_{i+1/2} - \alpha^n_{l,i}\right)H^*_{l,i+\frac{1}{2}} + \left(\alpha^n_{l,i} - \alpha^n_{l,i-1}\left(\frac{u_l^+}{|u_l|}\right)_{i-1/2} + \alpha^n_{l,i}\left(\frac{u_l^-}{|u_l|}\right)_{i-1/2}\right)H^*_{l,i-\frac{1}{2}}$$

and

$$F_{i+1/2}^{Lag,l}+F_{i-1/2}^{Lag,l}=\left(\frac{u_{12}^{*,-}}{\left|u_{12}^{*}\right|}\right)_{i+1/2}\mathrm{Max}\left(0,\alpha_{1,i}^{n}-\alpha_{1,i+1}^{n}\right)f_{12}^{Lag*}\left(w_{1,i}^{n},w_{2,i+1}^{n}\right)-\left(\frac{u_{21}^{*,-}}{\left|u_{21}^{*}\right|}\right)_{i+1/2}\mathrm{Max}\left(0,\alpha_{1,i+1}^{n}-\alpha_{1,i}^{n}\right)f_{21}^{Lag,*}\left(w_{2,i}^{n},w_{1,i+1}^{n}\right)$$
$$-\left(\frac{u_{12}^{*,+}}{\left|u_{12}^{*}\right|}\right)_{i-1/2}\mathrm{Max}\left(0,\alpha_{1,i-1}^{n}-\alpha_{1,i}^{n}\right)f_{12}^{Lag*}\left(w_{1,i-1}^{n},w_{2,i}^{n}\right)+\left(\frac{u_{21}^{*,+}}{\left|u_{21}^{*}\right|}\right)_{i-1/2}\mathrm{Max}\left(0,\alpha_{1,i}^{n}-\alpha_{1,i-1}^{n}\right)f_{21}^{Lag,*}\left(w_{2,i-1}^{n},w_{1,i}^{n}\right)$$

Let's consider the example of a flow at positive velocity at both cell boundaries. Moreover we assume a monotonic increasing volume fraction profile,

$$\alpha_{1,i-1}^{n}<\alpha_{1,i}^{n}<\alpha_{1,i+1}^{n}.$$

The former expressions reduce respectively to,

$$(\alpha H)_{1,i+\frac{1}{2}}^{*}-(\alpha H)_{1,i-\frac{1}{2}}^{*}-\alpha_{1,i}^{n}\left(H_{1,i+\frac{1}{2}}^{*}-H_{1,i-\frac{1}{2}}^{*}\right)=\left(\alpha_{1,i}^{n}-\alpha_{1,i-1}^{n}\right)H_{1,i-\frac{1}{2}}^{*},$$

and,

$$F_{i+1/2}^{Lag,l}+F_{i-1/2}^{Lag,l}=\left(\alpha_{1,i}^{n}-\alpha_{1,i-1}^{n}\right)f_{21}^{Lag,*}\left(w_{2,i-1}^{n},w_{1,i}^{n}\right).$$

In the present context, the only fluids contact to consider is contact 2-1. In this situation,

$$H_{1,i-\frac{1}{2}}^{*}=f_{21}^{Lag,*}\left(w_{2,i-1}^{n},w_{1,i}^{n}\right).$$

This example shows agreement between the discrete form $\alpha_{k,i}^{n}\left(H_{k,i+\frac{1}{2}}^{*}-H_{k,i-\frac{1}{2}}^{*}\right)$ and the DEM one.

It's easy to show that the example of a flow at negative velocity at both cell boundaries also shows agreement between $\alpha_{k,i}^{n}\left(H_{k,i+\frac{1}{2}}^{*}-H_{k,i-\frac{1}{2}}^{*}\right)$ and the DEM discrete form.

Finally, let's consider a more complicated type of flow. We assume a positive velocity at the left cell boundary, and a negative one at the right cell boundary. Besides we suppose the following volume fraction profile,

$$\alpha_{1,i-1}^{n}>\alpha_{1,i}^{n}<\alpha_{1,i+1}^{n}.$$

Thus, we obtain,

$$(\alpha H)_{1,i+\frac{1}{2}}^{*}-(\alpha H)_{1,i-\frac{1}{2}}^{*}-\alpha_{1,i}^{n}\left(H_{1,i+\frac{1}{2}}^{*}-H_{1,i-\frac{1}{2}}^{*}\right)=\left(\alpha_{1,i+1}^{n}-\alpha_{1,i}^{n}\right)H_{1,i+\frac{1}{2}}^{*}+\left(\alpha_{1,i}^{n}-\alpha_{1,i-1}^{n}\right)H_{1,i-\frac{1}{2}}^{*}$$

and,

$$F_{i+1/2}^{Lag,l}+F_{i-1/2}^{Lag,l}=\left(\alpha_{1,i+1}^{n}-\alpha_{1,i}^{n}\right)f_{21}^{Lag,*}\left(w_{2,i}^{n},w_{1,i+1}^{n}\right)+\left(\alpha_{1,i}^{n}-\alpha_{1,i-1}^{n}\right)f_{12}^{Lag*}\left(w_{1,i-1}^{n},w_{2,i}^{n}\right).$$

In the present context, the fluids contact to consider at the left boundary cell is contact 1-2. In this situation, $H^{*}_{1,i-\frac{1}{2}} = f_{12}^{Lag*}\left(w^{n}_{1,i-1}, w^{n}_{2,i}\right)$.

On the contrary, the fluids contact to consider at the right boundary cell is contact 2-1. We have too, $H^{*}_{1,i+\frac{1}{2}} = f_{21}^{Lag,*}\left(w^{n}_{2,i}, w^{n}_{1,i+1}\right)$.

All these flow configurations show agreement between the discrete form $\alpha^{n}_{k,i}\left(H^{*}_{k,i+\frac{1}{2}} - H^{*}_{k,i-\frac{1}{2}}\right)$ and the DEM one.

* A simple, robust and accurate HLLC-type scheme is built for non-equilibrium two-phase flows.
* The key point relies on local conservative formulation.
* The full system with seven equations is locally split in two subsystems with 4 waves in each phase.
* The solver is shown to be entropy preserving.
* Its implementation in existing codes is considerably simplified compared to the DEM.